AIAA JOURNAL
Vol. 48, No. 9, September 2010

Experimental and Numerical Fluid-Structure Analysis of Rigid and Flexible Flapping Airfoils

Stephan Bansmer* and Rolf Radespiel†
Technische Universität Braunschweig, 38106 Braunschweig, Germany
and
Ralf Unger,‡ Matthias Haupt,§ and Peter Horst¶
Technische Universität Braunschweig, 38108 Braunschweig, Germany

DOI: 10.2514/1.J050158

A combined experimental and computational study is presented for an airfoil undergoing a combined pitching and plunging motion at Reynolds number 100,000, where transition takes place along laminar separation bubbles. The numerical simulation approach addresses unsteady Reynolds-averaged Navier–Stokes solutions and covers transition prediction for unsteady mean flows. To study the effect of wing flexibility, the aerodynamic computational method is coupled with a structural solver using a Galerkin method. The numerical simulations are validated using high-resolution, phase-locked stereoscopic particle image velocimetry for one flapping case with a reduced frequency of $k = 0.2$. Hereby both a rigid and a flexible birdlike airfoil are investigated. The flow reveals strong unsteadiness resulting in moving laminar separation bubbles, both well captured by the numerical simulations performed in this study.

Nomenclature

A	=	amplitude of wave disturbance oscillation, m
c	=	airfoil chord length, m
c_d	=	drag coefficient, sum of $c_{d,f}$ and $c_{d,p}$
$c_{d,f}$	=	friction drag coefficient
$c_{d,p}$	=	pressure drag coefficient
c_l	=	lift coefficient
$\boldsymbol{d}^f$, $\boldsymbol{d}^s$	=	fluid and structural displacements, m
$\hat{\boldsymbol{d}}$	=	discrete displacement vector, m
$\boldsymbol{F}^f$, $\boldsymbol{F}^s$	=	fluid and structural forces, N
$\hat{\boldsymbol{F}}$	=	discrete force vector, N
f	=	frequency of the flapping motion, Hz
i	=	integer increment
j	=	imaginary unit, $j = \sqrt{-1}$
$\mathbf{K}$	=	stiffness matrix N/m
k	=	reduced frequency
M	=	number of samples
$\mathbf{M}$	=	mass matrix, kg
m	=	mass, kg
N	=	N factor
$\boldsymbol{N}$	=	shape functions
$\hat{\boldsymbol{p}}$	=	discrete pressure vector, N/m^2
Re	=	Reynolds number
T	=	period time of one flapping cycle, s
t	=	time, s
U_∞	=	freestream velocity, m/s
u, v, w	=	velocity components, m/s
u', v'	=	turbulence velocity components, m/s
$\boldsymbol{v}$	=	velocity vector
x, y, z	=	Cartesian coordinates, m
x_t	=	Cartesian coordinate of the transition location, m
x_0	=	Cartesian coordinate of the point of neutral stability, m
$\boldsymbol{x}$	=	vector of Cartesian coordinates
$\hat{z}$	=	plunging amplitude, m
α	=	complex wave number in x direction, 1/m
α_{eff}	=	effective angle of attack, deg
β	=	complex wave number in y direction, 1/m
Γ	=	surface
$\Delta\alpha_{\text{eff}}$	=	amplitude of the effective angle of attack, deg
$\Delta\Psi$	=	phase difference between pitch and plunge motion, deg
δ	=	variational operator
ζ	=	induced angle of attack due to plunge motion, deg
λ	=	Lagrange multiplier
σ_{xy}	=	turbulent shear stress, kg/(ms^2)
ϱ	=	density, kg/m^3
φ	=	pitch angle, geometric angle of attack, deg
φ_0	=	mean pitch, mean geometric angle of attack, deg
$\hat{\varphi}$	=	pitch amplitude, deg
Ω	=	domain
ω	=	complex frequency of disturbance wave, Hz
ω^f	=	vorticity, 1/s

Received 27 August 2009; revision received 9 March 2010; accepted for publication 10 March 2010.

*Research Engineer, Institute of Fluid Mechanics; s.bansmer@tu-braunschweig.de.

†Professor, Institute of Fluid Mechanics; r.radespiel@tu-braunschweig.de. Senior Member AIAA.

‡Research Engineer, Institute of Aircraft Design and Lightweight Structures; r.unger@tu-braunschweig.de.

§Senior Research Engineer, Institute of Aircraft Design and Lightweight Structures; m.haupt@tu-braunschweig.de.

¶Professor, Institute of Aircraft Design and Lightweight Structures; p.horst@tu-braunschweig.de.

I. Introduction

WE PRESENT comparisons between experimental and computational results of a nominally two-dimensional flapping airfoil at low Reynolds numbers. The flapping motion is prescribed by a combined plunging and pitching motion with a phase difference of 90 deg. Inspired by the aerodynamics of flapping flight [1–3] of birds, a fundamental question is to understand the influence of structural wing flexibility on the aerodynamic performance. According to Heathcote and Gursul [4], a certain degree of flexibility seems to increase both thrust coefficient and propulsive efficiency for a generic airfoil in a teardrop/flat plate design, see Fig. 1. Furthermore, De Luca et al. suggested a better performance for a micro air vehicle (MAV) configuration with flexible wings [5]. However, the authors were not able to identify the aerodynamic source for the increased L/D values. This is indeed not a simple question because

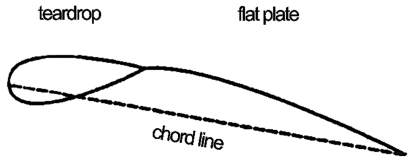

Fig. 1 Sketch of the generic airfoil by Heathcote and Gursul [4].

even in generic two-dimensional test cases many effects like moving laminar turbulent transition [6,7], vortex shedding [8,9], and multimodal structural deformations [10] are influencing each other.

The laminar-turbulent transition in this Reynolds number range takes place along laminar separation bubbles (LSB). Figure 2 describes the physics of a LSB. The oncoming laminar boundary-layer separates, which is caused by a pressure increase along the airfoil contour. According to Spalart and Strelets [11] and Rist [12], the separated flow performs the transition process from laminar to turbulent flow following a gradual development of the primary instabilities from Tollmein–Schlichting instabilities toward Kelvin–Helmholtz instabilities [13]. The resulting turbulent fluctuations in the flow enhance momentum transport toward the wall, and the flow reattaches to the airfoil contour. The resulting region of circulating flow is called the LSB. LSBs are usually not desired in airfoil design because they increase the pressure drag of the airfoil due to a higher displacement thickness level of the boundary layer.

In this contribution, we want to provide validated and efficient numerical tools, which cover all the above-mentioned challenges of fluid-structure interactions at transitional low Reynolds numbers. This is done in three steps:

1) *Generating an Airfoil*: We want to draw on naturally evolved airfoils. Therefore, the shape of the hand pinion of a seagull was our design paradigm, also because the hand pinion of bird wings is known to be the thrust producing part [14], which is favorable for future MAV design. As a result, the SG04 airfoil was developed;

2) *Defining the Approach and Setting up Numerical Simulations*: To understand the influence of flexibility, a comparison between a flexible and a rigid SG04 airfoil is necessary. This comparison, with its optimization problem of maximizing the propulsive efficiency, can only be done economically by means of computational methods. For the aerodynamics of the rigid airfoil, the validation of the transition prediction is of particular interest. In this connection, Radespiel et al. [7] contributed a generalized e^N method for a flapping SD7003 airfoil. To simulate flow phenomena interacting on a highly-flexible thin structure and involving laminar separation bubbles, high qualitative and time resolved coupling schemes for fluid-structure interaction problems are adopted [10,15]. Using a partitioned coupling approach, well-validated fluid as well as structural solvers are linked together in a simulation environment with the aid of flexible data transfer libraries [16]. Three coupling aspects need to be addressed: the data transfer across nonmatching interface grids, the time integration and equilibrium iteration of the whole coupled system and the grid deformation of the fluid grid to take the updated geometry into account. For the first aspect, a conservative data transfer scheme based on the Lagrange multipliers and the Galerkin discretization is developed. Further, the flow solver needs the capability to solve the governing equation on moving grids;

3) *Validation Case*: The computational methods have to be validated. Therefore, rigid and flexible models of the SG04 airfoil were manufactured in lightweight design. High-resolution particle image velocimetry (PIV) of the boundary layer was used to capture velocity fields and turbulent shear-stress distributions around the airfoils. Investigations were performed both for steady cases at constant angle of attack and for an unsteady case with the oscillating airfoils at a reduced frequency of $k = 0.2$. To capture structural modes of the flexible airfoil, deformation measurements were applied.

II. Birdlike Airfoils

A. Aerodynamic Design

Compared with conventional airfoils, two major design aspects can be found when examining the airfoil of a seagull in the vicinity of its hand pinion: first, a large maximum camber compared with artificial airfoils, and second, the position of maximum thickness is situated close to the leading edge, see also Fig. 3.

There are several reasons why the position of maximum thickness is located near the leading edge. Considering the wing anatomy, the skeleton and muscles run in this section, whereas at the trailing-edge region of the airfoil, only the feathers determine the airfoil shape. From an aerodynamic point of view, there are also advantages of this design. On the one hand, the adverse pressure gradients along the upper surface can be kept reasonably small. This yields thin laminar separation bubbles with low-pressure drag losses, which can be seen in the drag polar of the airfoil discussed later on in Sec. VI.A.2. On the other hand, thin airfoils have normally a small range of applicable angles of attack where no stall occurs. Airfoils with their position of maximum thickness in the vicinity of the leading edge exhibit an increased nose radius, which results in a relatively large angle of attack range with attached flow.

A large relative camber of 8% was measured by BILO using narcotized birds [17]. However, observations in nature revealed that this value is usually smaller for gliding flight, although in wind-tunnel experiments with living birds the maximum camber during one flapping stroke was found to vary from 8 to 12%.

Based on these design aspects, a new birdlike airfoil, the SG04, was developed [18], see Fig. 4. This profile has a maximum thickness and a maximum camber of 4%, where the maximum camber is located at $x/c = 40\%$. At operational angles of attack between 0 and

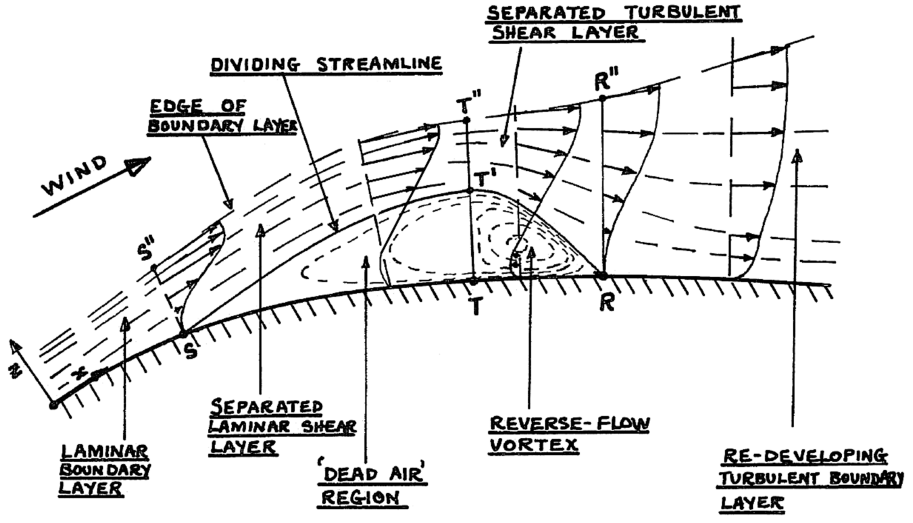

Fig. 2 Sketch of a LSB by Horton [40] *(corrected)*.

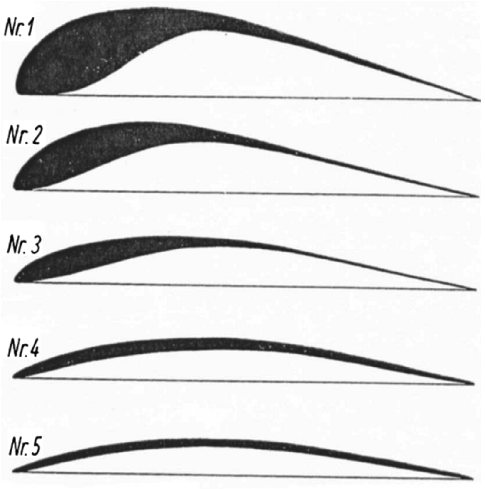

Fig. 3 Comparitative investigations on airfoil shapes of birds from Oehme [41]. Shown are five idealized bird wing sections.

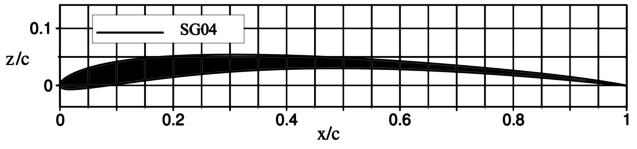

Fig. 4 The birdlike airfoil SG04.

8 deg, the lift coefficient has values of about 0.5 up to 1.2, see also Sec. VI.A.2. The aerodynamic design of the SG04 involved both aerodynamic analysis and inverse design according to the bubble ramp approach introduced by Selig [19] to reduce the size of the laminar separation bubble for a broad range of angles of attack.

B. Airfoil Manufacturing

To determine the influence of the airfoil flexibility on the aerodynamic efficiency, two airfoil models had to be manufactured, one rigid and one flexible. The rigid airfoil was made of a carbon-fabrics shell, which was reinforced by a closed-cell rigid foam. For a high bending stiffness, a carbon fiber spar was integrated. A top coat out of polyester resin provided a smooth surface, see Fig. 5.

To adapt the wing of birds in an engineering way for this two-dimensional application, several lightweight concepts were evaluated to find a design satisfying the following requirements for the flexible airfoil: 1) an area weight close to bird's feathers, 2) deformation due to aerodynamic and inertia loads should be in same range, to equally consider both sources of deformation, 3) preservation of a 2-D behavior, 4) smooth surface shape for PIV measurements, and 5) simple manufacturing.

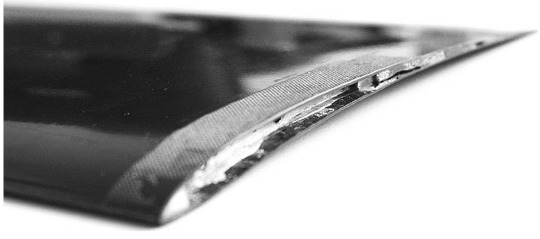

Fig. 5 The rigid birdlike airfoil SG04 in lightweight design.

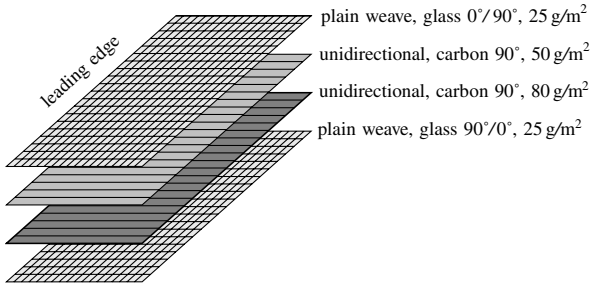

Fig. 7 Layer structure of the shells (angles are taken to the leading edge/*y* direction).

Clearly, the second requirement is for validation purposes rather than taken from nature. As for the rigid airfoil, the dimension of the manufactured model needs to meet the wind-tunnel requirements. Therefore the dimensions of the manufactured model's area is 398 mm × 200 mm (span × chord). A design using carbon-reinforced plastic with a stiff forebody and an overlapping three-shell concept was found to be a reasonable approach for the flexible airfoil, Fig. 6a. The upper and lower shell are bonded together at the leading edge and prestressed to ensure continual contact during a flapping period, while the central shell is attached to a stiff spar also made by carbon fiber reinforced composites. A shell thickness of 0.15 mm and a layer structure according to Fig. 7 give reasonable deflections of the trailing edge due to aerodynamic forces and the structure itself retains a good two-dimensional behavior. Further, at 65% of the chord length, the upper and lower shell are in contact with the central shell. This gives reasonable deflection in terms of the second requirement, as mentioned above. The total mass of this lightweight configuration is $m = 124$ g including the metal parts, e.g., ribs for the wind-tunnel mounting.

With the technology used in this study, these flexible shells are still more flexible than, e.g., overlapping feathers of a pigeon, while the mass of the shells is slightly higher than that measured for a pigeon feather compound. Furthermore, it should be noted here that the three-shell concept is a two-dimensional engineereering adaptation of the more sophisticated bird's wing structure and is therefore not useful for analyzing full three-dimensional flapping flight. However, the flexible shell concept can be used to validate the coupled problem where a flexible airfoil is deformed under aerodynamic and inertial loads. The numerical model can then be used to simulate the flow around the structure, which is even more realistic in terms of overlapping feathers, e.g., tapered shells with a keratin density.

To validate a numerical model of the manufactured airfoil the first eigenform and eigenfrequency was experimentally investigated with the aid of an optical three-dimensional deformation analysis system (ARAMIS) using a stochastic pattern as well as a laser sensor, which uses optical triangulation as a measuring principle at certain points [20].

C. Kinematics of the Oscillating Airfoil

In this contribution, the two-dimensional case of an oscillating airfoil is discussed. The motion is combined by a plunging $z(t/T)$ motion of the quarter chord point and a pitching oscillation $\varphi(t/T)$ around the quarter chord for one flapping period $0 \leq t/T < 1$:

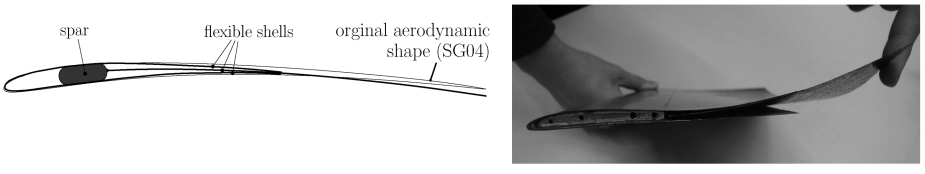

a) Principle design **b) Manufactured flexible airfoil**

Fig. 6 Design of the flexible airfoil.

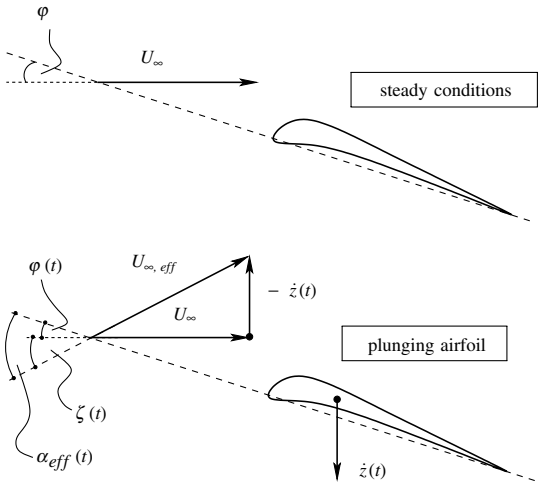

Fig. 8 The change from geometric φ to effective angle of attack $\alpha_{\text{eff}}(t)$ due to the plunging motion $\dot{z}(t)$.

$$z(t/T) = \hat{z} \cdot \cos(2\pi t/T)$$
$$\varphi(t/T) = \hat{\varphi} \cdot \cos(2\pi t/T + \pi/2) + \varphi_0 \quad (1)$$

These motions influence the local oncoming flow conditions in the frame of reference of the airfoil. For example, if the airfoil under freestream conditions moves downwards, the airfoil in its frame of reference is exposed with an additional flow component in the upward direction.

Consequently, the oncoming flow vector changes direction and magnitude, see Fig. 8. This has also an impact on the local angle of attack. The geometric angle of attack φ is superimposed by the induced angle of attack ζ resulting from the plunging motion of the airfoil, which finally yields to the effective angle of attack α_{eff}

$$\alpha_{\text{eff}}(t/T) = \varphi(t/T) + \zeta(t/T) = [\hat{\varphi} \cdot \cos(2\pi t/T + \pi/2) + \varphi_0] + \left[\arctan\left(-\frac{1}{U_\infty} \cdot \frac{\partial z(t/T)}{\partial t}\bigg|_{x=\frac{c}{4}}\right)\right] \approx \Delta\alpha_{\text{eff}} \cdot \sin(2\pi t/T) + \varphi_0 \quad (2)$$

The pitching motion affects similarly the oncoming flow vector. However, its induced flow velocity in the z direction is a function of the distance to the rotational axis of the pitching motion. Hence, this influence can be interpreted as a decambering of the airfoil.

Often, the reduced frequency k is introduced, given by

$$k = \frac{\pi f c}{U_\infty} \quad (3)$$

The inverse of k is a measure how far the undisturbed air passes the airfoil during one flapping cycle. Therefore, the reduced frequency can be used to classify the level of aerodynamic unsteadiness. For seagull flight conditions, k has values around 0.2. This can be derived from cruising flight data of birds, see Pennycuick [21] and Herzog [22]. According to this data, a kelp gull (larus dominicanus) has a mean chord length of 0.16 m and a flapping frequency of 3.46 Hz. Assuming a cruise speed of 8 m/s, the reduced frequency can be determined to be $k = 0.22$. Insects are known to have a reduced frequency of about 1.0 [23].

III. Experimental Investigations

There are two aims of the experimental investigations. The first objective is to capture the flowfield in the boundary layer of the oscillating airfoils and its turbulent quantities like the turbulent shear stress. Secondly, we aim to determine the deformation of the flexible airfoil during one flapping cycle. Later on, these quantities will be used to compare them with numerical computations. In other words, the measurements carried out serve as a validation case and not prescribing a database for parametric studies.

A. Wind Tunnel

The experiments were carried out at the low-speed Low-Noise Wind Tunnel, see Fig. 9. The inlet of the Eiffel-type tunnel is covered by a fleece mat 30 mm in thickness. Afterward, the air passes a straightener made out of aluminum honeycombs, 14 mm in diameter and 200 mm in length and then finally through a fine-mesh woven screen. In the large settling chamber, small-scale turbulence is dissipated, and a Boerger-type nozzle contracts the air at a 16:1 ratio. Consequently, the air has a very low turbulence level in the 400 × 600 millimeter sized test section. The wind tunnel is driven by a 4 kW, acoustically encapsulated, speed controlled three-phase asynchronous motor, which produces stable wind-tunnel speeds from 2 up to 20 meters per second. The diffuser is mounted on a rail system, which allows one to interchange modular test sections. The laboratory is lined with open-celled acoustic foam.

B. Motion Apparatus

To create a combined plunging and pitching motion of the airfoil as denoted by Eq. (1), the Flapping Flight Motion Apparatus was used. The apparatus was designed and manufactured at the Institute of Fluid Mechanics [18]. A broad range of motion parameters can be adjusted: plunging amplitude from 0 to 0.1 meters, pitching amplitude from 0 to 25 deg, flapping frequency from 0 to 10 Hertz. Additionally, a light barrier is mounted at the rig enabling the connected measurement systems to be triggered according to the operated flapping frequency. The estimated motion accuracy for the validation case averages to 0.8 mm for the plunging motion and to 0.2 deg for the pitching motion. The accuracy was measured by capturing the airfoil position at a constant phase for 500 flapping cycles and determining its standard deviation.

C. PIV Measurements

The stereoscopic Particle Image Velocimetry (PIV) was chosen to capture the flowfield in the boundary layer of the flapping airfoil. The

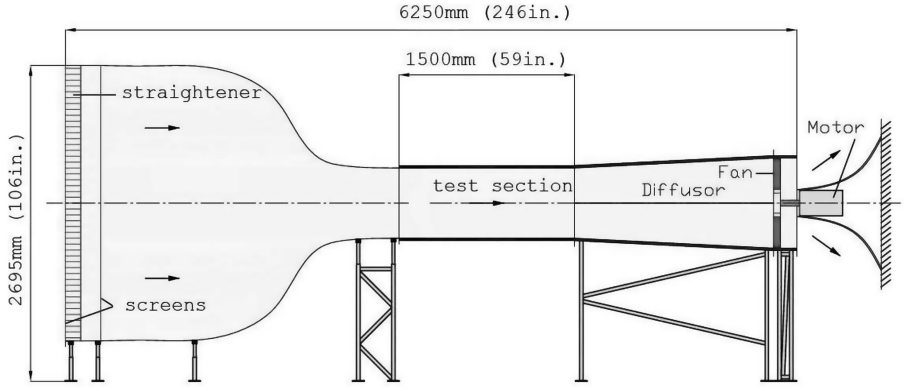

Fig. 9 Schematic of the low-speed Low-Noise Wind Tunnel.

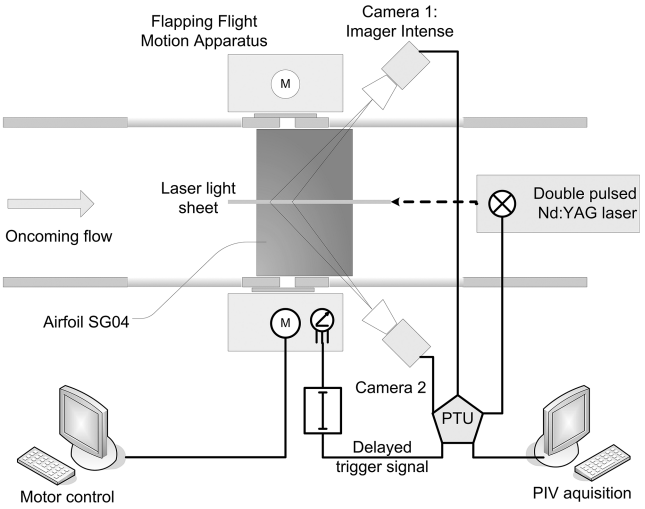

Fig. 10 The stereoscopic PIV setup as a top view.

advantage of this nonintrusive measurement technique is not only to gather a complete velocity field instead of pointwise information, but also to obtain quantitative data with reasonable accuracy [24]. The detailed setup is sketched in Fig. 10 as a top view of the wind-tunnel test section. The oncoming flow from left passes the moving airfoil, which is driven by the motion apparatus outside the test section. A double-pulsed Nd:YAG laser (Quantel Brilliant, energy: 2×150 mJ, wavelength: 532 nm) mounted on the top of the wind tunnel creates a thin light sheet in the chordwise direction. Two cameras capture images of the illuminated tracer particles (oil particles with a mean diameter of about 1 μm). Two different camera types were used during the measurements: LaVision Imager Intense and LaVision Imager pro X 11M. The stereoscopic setup was necessary because the Flapping Flight Motion Apparatus does not allow for direct visible access normal to the laser light sheet, i.e., no standard PIV was possible. It should be mentioned that the field of view of the cameras was only 2.5×2 cm^2, otherwise there would not be sufficient resolution to capture the boundary-layer flow, see also Fig. 11. These dimensions are very small compared with the airfoil chord length of 20 cm. Hence, the camera system had to be attached to a translation device to move the system in plunging and chordwise direction without changing the alignment of the cameras. To capture the flowfield at a constant phase angle, phase-locked imaging was performed. For this purpose, a TTL signal from the Flapping Flight Motion Apparatus, which triggers at the beginning of each flapping cycle, was captured and shifted in time by a Stanford delay generator DG 535. When the delayed signal was detected by the Programmable Timing Unit (PTU9 by LaVision), the laser flash and the camera exposure was initiated. The PIV system was controlled by the Davis Software of LaVision. The sampling rate was adjusted to one particle image pair per flapping cycle.

Once the particle image acquisition of at least 500 image pairs for each of the independently captured measurement windows was completed, the velocity vector field of the flow around the airfoil and its turbulent quantities were determined. First of all, a wobble correction was performed as follows. When the laser light sheet touched the airfoil surface, the so-called reflection line was A visible on the camera images. The thickness of this reflection line varied from 3 to 40 pixel depending on the local curvature of the airfoil. Because of the phase-locked imaging, this reflection which indicates

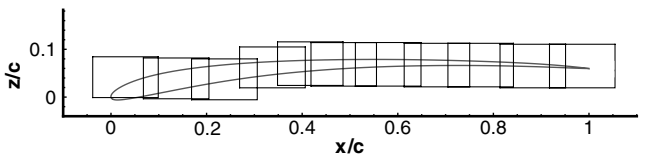

Fig. 11 Eleven measurement windows were used to capture the boundary layer of the flapping SG04 airfoil.

the position of the airfoil should be always at the same location. However, the reflection line is wobbling about fractions of 1 mm in the camera images. This wobbling had to be removed: for the later ensemble averaging procedure of the vector fields (to compute the mean flow vector field, et cetera), the airfoil has to be at the same position. Having performed several image preprocessing techniques to improve the particle image quality, the particle displacement evaluation was done in a next step using a cross correlation scheme. A multipass interrogation scheme with decreasing interrogation window size (from 128×128 pixels down to 32×32 pixels), 50% overlap and elliptical weighting function was applied.

The resulting set of at least 500 vector fields for each measurement window was post-processed afterwards. This was mandatory to filter out nonphysical vectors, which would impair the results of the ensemble averaging procedure. Ensemble averaging is the statistical task to compute the mean velocity field, as given by the equation:

$$\langle \boldsymbol{v}(\boldsymbol{x},t)\rangle = \begin{pmatrix} \langle u(\boldsymbol{x},t)\rangle \\ \langle v(\boldsymbol{x},t)\rangle \\ \langle w(\boldsymbol{x},t)\rangle \end{pmatrix} = \frac{1}{M}\sum_{i=1}^{M} \boldsymbol{v}_i(\boldsymbol{x},t)$$

Moreover, the turbulent shear stress σ_{xz} can be computed [25]

$$\sigma_{xz} = -\varrho \cdot \langle u' \cdot w'\rangle = -\varrho \cdot \frac{1}{M}\sum_{i=1}^{M}(u_i - \langle u\rangle)(w_i - \langle w\rangle) \quad (4)$$

Finally, all measurement windows per investigated phase angle were placed at the correct position on the airfoil to obtain the complete distribution of the computed quantities along the airfoil surface. This operation was done with TECPLOT 360.

D. Deformation Measurements

The deformations of the flexible airfoil were measured in two ways. First with a commercially available optical 3-D deformation system (ARAMIS), which uses a stochastic pattern painted onto the specimen's surface. A cross correlation scheme is then used to compute the deformations. For the image acquisition, individual synchronized stereo images of the pattern are recorded at different load stages using charge-coupled device cameras and during an image processing step, the 3-D coordinates and 3-D displacements are postprocessed automatically by the system.

Secondly, a custom made deformation measurement was performed with the stereoscopic PIV equipment, see Fig. 12. A stochastic pattern was again painted on the airfoil surface. Two Imager Intense cameras from LaVision were arranged to obtain stereoscopic imaging. Unlike the calibration procedure with the commercial deformation measurement system, a more precise method was used to map the camera images, i.e., for each phase a calibration was performed. Therefore, the calibration grid was moved directly to the phase position of the airfoil and consequently, the observed measurement volume was better resolved. 100 phase-locked images

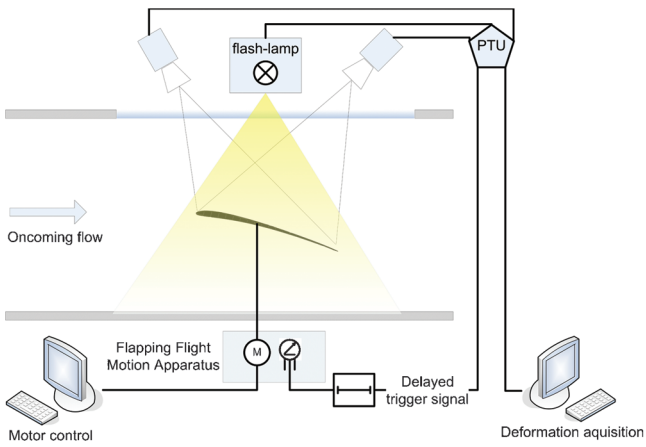

Fig. 12 Setup of the custom made deformation measurement system.

of the flapping airfoil with the stochastic pattern were captured for statistical purposes. The sampling rate was adjusted to one image per flapping cycle. To illuminate the stochastic pattern on the airfoil during the image acquisition, a commercially available flash-lamp was used. The images were cross-correlated with the jig shape of the airfoil at the same phase position using a multipass interrogation scheme with decreasing interrogation window size (from 256×256 pixels down to 64×64 pixels), 50% overlap and elliptical weighting function. In this setup, the wobbling correction was performed by subtracting the deformation vector of the quarter chord line, where the stiff forebody of the flexible airfoil is connected to the motion apparatus, from the whole instantaneous deformation vector field. Afterwards, the ensemble averaged deformations were used for further analysis.

IV. Numerical Simulation of the Rigid Airfoil

The numerical simulation approach is based on unsteady Reynolds-averaged Navier–Stokes (URANS) solutions, which are coupled with a sound transition prediction method. Details of this approach can be found in Radespiel et al. [7]. This chapter only focuses on a brief overview of this methodology.

A. Simulation Approach

These low Reynolds number flows with laminar separation bubbles were computed using the unsteady Reynolds-averaged Navier–Stokes (RANS) equations. Linear stability analysis (LST), which investigates directly the velocity profiles of the RANS solution was then applied [25]. Waves due to Tollmien–Schlichting and Kelvin–Helmholtz instabilities were predicted by the stability analysis [12]. The amplification rates were then used to predict the transition location using an integration scheme for mode amplitude ratios that takes unsteady flow effects into account. The largest amplitude exponents were finally compared with a critical N factor to determine the transition location.

B. Navier–Stokes Code FLOWer

The Navier–Stokes solver FLOWer [26] requires block-structured meshes; its discretization scheme is a finite-volume approach. A second-order accurate central-difference scheme with scalar dissipation was applied to evaluate convective fluxes. Implicit residual smoothing, local time stepping, preconditioning and multigrid operations were performed to accelerate the computation. A second-order accurate implicit dual time stepping scheme was used for the time-accurate computations. The Menter-Baseline (BSL) k-ω-model [27] was chosen for the turbulence modeling. Its equations are not computed with multigrid acceleration techniques.

C. Linear Stability Analysis with LILO

To quantify the local amplification of disturbances, the stability equations of the laminar boundary layer are solved. LILO [28] treats laminar compressible boundary layers; here its option of assuming parallel flow is used. The harmonic-wave assumption is applied to the velocity components u, v, w as well as for static pressure p and temperature T, given exemplarily by the relation

$$q = \tilde{q}(x, y, z, t) + q'(x, y, z, t)$$
$$q'(x, y, z, t) = \hat{q} \exp(j(\alpha x + \beta y - \omega t)) \tag{5}$$

Assuming the frequency of the temporal distribution of the basic flow state is much smaller than the frequency of the single wave mode, the time dependence of the evolution matrices of the system of five stability equations vanishes. Consequently, the stability problem can be solved at a discrete time. LILO computes the complex eigenvalue ω of the temporal stability problem in which the user has to specify the real wave numbers α and β for 3-D cases.

D. Transition Prediction

In many cases, the location of the final laminar breakdown to turbulence is dominated by the behavior of the primary instabilities with their exponential growth. It was found that the point where the boundary layer becomes fully turbulent correlates well with a certain amplification factor of the most unstable primary wave that is calculated from the point of neutral stability x_0. These findings constitute the e^N method [29]. A suitable mathematical formulation of this method can be derived from the kinematic wave theory [30]. Disturbance waves with discrete wave frequencies are assumed to travel downstream and to grow exponentially. Having calculated the amplification of these waves

$$A(x) = A_0 \cdot \exp\left(- \int_{x_0}^{x} \alpha_i \, \mathrm{d}x \right) \tag{6}$$

one can extract the so-called N factor by taking the maximum value of the amplitude exponent

$$N(x) = \max_{\omega} \left[- \int_{x_0}^{x} \alpha_i(x, \omega) \, \mathrm{d}x \right] \tag{7}$$

and then compare this value with a critical N factor, which yields to the transition location. While this formulation has been applied in steady flow cases for many years, a new unsteady integration scheme for N factors was introduced by Radespiel et al. [7] by using the temporal evolution of amplification rates over time and space to compute suitable N factors along the airfoil surface for unsteady flow problems. Details of the formulation and its numerical implementation are given in [7,31]. For low reduced frequencies, the steady transition prediction is sufficiently precise [32], and will be applied in most of the cases in the present contribution.

V. Numerical Simulation of the Flexible Airfoil

Because of the nonlinearities of the fluid-structure interaction problem, the aforementioned URANS solver including the transition prediction algorithm is fully coupled to a structural solver, which uses the spatial finite element discretization for the flexible airfoil. The physical system is treated in the time domain using the Newmark

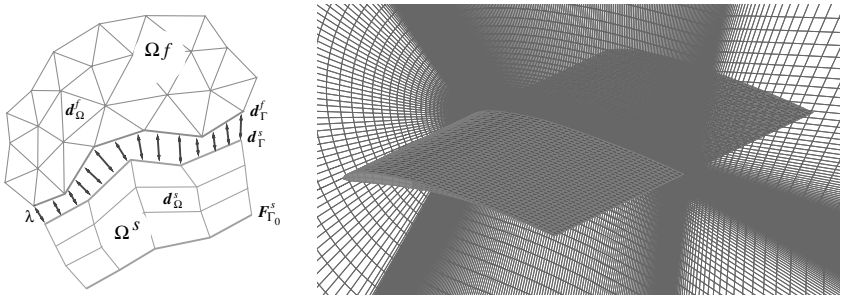

a) Coupling of the fluid and the structure

b) Structural and fluid grid

Fig. 13 Coupled computational domains.

time integration on the structural side of the coupled system. The motion described in Eq. (1) is applied at the quarter chord line of the structural model. The basic partitioned coupling approach is nowadays widely used for computational aeroelasticity [33] and some of the numerical elements used and added in this work are discussed in the next subsections.

A. Data Interpolation

In general, the data transfer takes place across nonmatching interface grids, schematically depicted in Fig. 13a. The grids used for the fluid and structural domain are shown in Fig. 13b. From the continuum mechanics point of view, the structural part of the coupled problem deform with a displacement field $\boldsymbol{d}^s_\Omega = [d^s_{\Omega,x}, d^s_{\Omega,y}, d^s_{\Omega,z}]^T$ due to the boundary loads $\boldsymbol{F}^s_{\Gamma_0} = [F^s_{\Gamma_0,x}, F^s_{\Gamma_0,y}, F^s_{\Gamma_0,z}]^T$ and $\boldsymbol{\lambda}$. The Lagrange multiplier field $\boldsymbol{\lambda} = [\lambda_x, \lambda_y, \lambda_z]^T$ has the physical meaning of a force flux gluing both subdomains together at the interface Γ. A weak formulation of the continuity transfer condition is used:

$$\boldsymbol{d}^s_\Gamma = \boldsymbol{d}^f_\Gamma \rightarrow \int_\Gamma \boldsymbol{\lambda}^T(\boldsymbol{d}^s_\Gamma - \boldsymbol{d}^f_\Gamma)\,\mathrm{d}\Gamma = 0 \tag{8}$$

where $\boldsymbol{d}^s_\Gamma$ and $\boldsymbol{d}^f_\Gamma$ are the structural and fluid displacements defined on the coupling interface Γ, and $\boldsymbol{\lambda}$ is again the Lagrange multiplier, which act as a jump weight of the interface state variables. The two way coupling of the fluid and the structure is then explained, that the structural displacements $\boldsymbol{d}^s_\Gamma$ on the common interface Γ influences the fluid boundary displacements $\boldsymbol{d}^f_\Gamma$ via the Lagrange multiplier $\boldsymbol{\lambda}$. A new location of the fluid domain needs to be evaluated with the aid of $\boldsymbol{d}^f_\Omega$ and the new fluid domain finally leads to updated values for $\boldsymbol{\lambda}$.

By using the Galerkin method and shape function for the discrete interface state variables, $\boldsymbol{d}^i_\Gamma = \boldsymbol{N}^i_d \hat{\boldsymbol{d}}^i_\Gamma$, the Lagrange multiplier needs to be discretized in a way that the resulting scheme is uniquely solvable for the nodal values of the fluid interface displacements $\hat{\boldsymbol{d}}^f_\Gamma$ and therefore the shape functions of the Lagrange multiplier are chosen to be the same as for the displacements of the fluid interface, $\boldsymbol{N}_\lambda = \boldsymbol{N}^f_d$. The discretized version of Eq. (8) then reads

$$\mathbf{M}_{ff}\hat{\boldsymbol{d}}^f_\Gamma = \mathbf{M}_{fs}\hat{\boldsymbol{d}}^s_\Gamma \quad \text{with} \quad \mathbf{M}_{fi} = \int_\Gamma \boldsymbol{N}^{f^T}_d \boldsymbol{N}^i_d\,\mathrm{d}\Gamma \tag{9}$$

which has to be solved for $\hat{\boldsymbol{d}}^f_\Gamma$. The coupling matrices $\mathbf{M}_{ff}$ and $\mathbf{M}_{fs}$ are evaluated with the aid of a quadrature rule [10].

The corresponding load transfer is obtained by using the transposed relation of the state transfer. With the principle of virtual work and the displacement

$$\delta\hat{\boldsymbol{d}}^{f^T}_\Gamma \hat{\boldsymbol{F}}^f_\Gamma = \delta\hat{\boldsymbol{d}}^{s^T}_\Gamma \hat{\boldsymbol{F}}^s_\Gamma \rightarrow \hat{\boldsymbol{F}}^s_\Gamma = \mathbf{M}^T_{fs}\mathbf{M}^{-1}_{ff}\hat{\boldsymbol{F}}^f_\Gamma = \mathbf{M}^T_{fs}\hat{\boldsymbol{p}}^f_\Gamma \tag{10}$$

where the forces due to friction of the fluid flow are neglected and the nodal pressure values of the fluid $\hat{\boldsymbol{p}}^f_\Gamma$ are directly used.

B. Deformation of the Grid

The fluid grid needs to be deformed to take the new structural displacements into account. Here, the grid is treated as a pseudo-structural system, where the fluid interface displacements are applied as Dirichlet boundary conditions on this system:

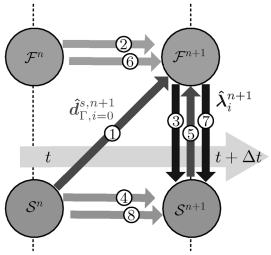

Fig. 14 Time integration scheme, where $\mathcal{F}$ and $\mathcal{S}$ stands for the fluid and structural solver, respectively (numbers indicates the sequence of processing steps).

$$\underbrace{\begin{bmatrix}\mathbf{K}^f_{\Omega\Omega} & \mathbf{K}^f_{\Omega\Gamma}\\ \mathbf{K}^f_{\Gamma\Omega} & \mathbf{K}^f_{\Gamma\Gamma}\end{bmatrix}}_{\mathbf{K}}\begin{bmatrix}\hat{\boldsymbol{d}}^f_\Omega\\ \hat{\boldsymbol{d}}^f_\Gamma\end{bmatrix} = \begin{bmatrix}\mathbf{0}\\ \mathbf{0}\end{bmatrix} \tag{11}$$

which has to be solved for $\hat{\boldsymbol{d}}^f_\Omega$. The stiffness for each finite element E^f_i is evaluated as the inverse of the minimal edge length and thus

$$E^f_i = \frac{1}{\min(e_{i,s})}; \qquad s = 1\ldots4 \tag{12}$$

where $e_{i,s}$ is the length of the sth edge for the cell i. Thus smaller cells near the wall have a higher stiffness than greater cells in the far field. The matrix $\mathbf{K}$ needs to be evaluated only once at the beginning of the computation and here the fluid grid is treated with plane elements. Further it should be noted here that due to the grid deformation the ALE-version of the Navier–Stokes and the turbulence equations need to be solved to account for the grid velocities and the resulting additional fluxes.

C. Equilibrium Iteration and Time Integration

Because of the use of a partitioned solution procedure, the nonlinear coupled system is solved by an iterative solution procedure. Using the fluid solver as described above and a structural solver, which solves the structural equation by the aid of the nonlinear finite element method to get the structural displacements on the interface from prescribed nodal forces, the coupled problem is solved during a time increment Δt by the classical Dirichlet–Neumann step. Here, the structural interface state $\hat{\boldsymbol{d}}^s_\Gamma$ is transferred to the fluid side, followed by the grid deformation and solving of the fluid problem. This is then followed by the load transfer and solving of the structural problem to get a new structural interface state, see Fig. 14. Underrelaxation and the use of a proper structural state predictor for the next time level is used to reduce the number of required equilibrium iterations, see [33] for details.

VI. Results

A. Rigid Airfoil

1. *Verification of Numerical Simulations*

Results of the verification [7,32] and validation [7,32,34] for the case with a SD7003 airfoil and steady oncoming flow have already been published. Validation cases for an oscillating SD7003 airfoil can be found in Radespiel et al. [7] and Windte and Radespiel[31]. In this section, only a brief overview will be given to verify the numerical simulations of the new birdlike SG04 airfoil.

The computational mesh for the numerical investigation of the SG04 airfoil contains 1088×224 cells on the finest grid level (L1). However, most computations were carried out on the second grid level with 544×112 cells (L2). To capture the expected laminar separation bubbles on the airfoil, the grid was adapted to a boundary-layer resolution of about 70 cells. Figure 15 shows the mesh on the third level (L3) in the vicinity of the airfoil. The far-field distance is about 20 times the chord length.

To simulate incompressible flow, the freestream Mach number was set to 0.05 and low-speed preconditioning was performed. A dual time stepping approach was used to compute time-accurate solutions. For the steady-state solutions, the time step was adjusted in a way that the oncoming flow would need 33 time steps to pass one chord length. Figure 16 depicts the influence of the grid resolution on lift and drag at a constant angle of attack of 6 deg. The grid level 2

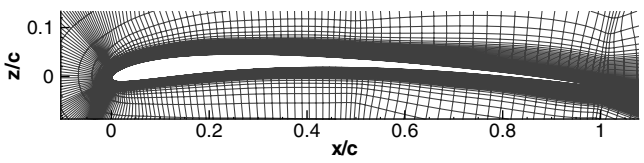

Fig. 15 Computational mesh of the SG04 airfoil on multigrid level 3 with 272×56 cells.

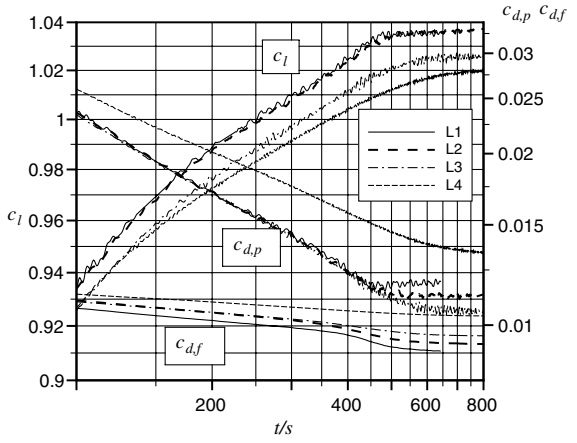

Fig. 16 Convergence of lift and drag for different grid resolutions, steady conditions, $Re = 100000$, AoA = 6 deg; note L1 is the finest level with 1088 × 224 cells.

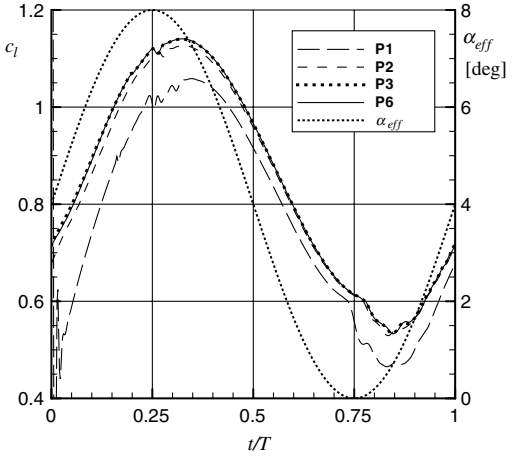

Fig. 18 Convergence of lift over physical time; flapping motion with $k = 0.2$, $Re = 100000$.

with 544 × 112 cells was found to be sufficient to determine the lift coefficient precisely. To run drag computations with an error of less than 1%, the finest grid had to be used.

For the case of the oscillating airfoil, the effect of the physical time step on the solution was investigated on grid level 2 (544 × 112 cells), as shown in Fig. 17. Lift, drag and transition location are plotted against the nondimensional time, starting with $t/T = 0$ at the top dead center of the flapping motion. The steady transition prediction scheme was applied, the critical N factor was set to 8 to guarantee a robust computational stability for the extensive parametric studies. All distributions match fairly well, i.e., a resolution of 500 physical time steps per flapping period seems sufficient. However, there are some small discrepancies at the middle of the downstroke at $t/T = 0.25$ in the lift distribution, which exhibit some minor oscillations for the case of 500 physical time steps per flapping period. This is because the steady transition module lets the transition move too early to the leading edge during the downstroke. This causes an early reattachment of the large laminar separation bubble while its remainings are washed away downstream as small vortices. Consequently, 1000 or even 2000 time steps per period resolve the physics of the transition movement more precisely and the lift oscillations fade away.

Figure 18 highlights exemplarily the lift convergence of one solution with 500 physical time steps per period. Having passed the third period, the FLOWer code delivers converged results for lift.

A final study was carried out regarding the grid convergence, see Fig. 19. The coarsest grid level 3 with 272 × 56 cells can only deliver a rough sketch of the aerodynamic coefficients during one flapping cycle. Especially the relaminarization during the upstroke ($0.5 \leq t/T < 1$) is poorly resolved.

Conversely, the finest grid level has the smoothest distributions for lift, drag and transition. However, with its computational effort of two weeks on a AMD opteron processor with 2.6 GHz, the calculation could not be used for extensive parametric studies. A good compromise was the usage of grid level two. Its computational effort is about three days combined with a reasonable agreement with the solution on the finest grid level.

2. *Results for Steady Conditions*

The numerical simulations for steady-state oncoming flow were carried out at $Re = 100000$ and at a freestream Mach number of 0.05 on grid level 2 with 544 × 112 cells. The critical N factor was set to 10 corresponding to experience with the wind tunnel and its low turbulence level. However, to demonstrate its influence on the aerodynamic performance, calculations with critical N factors of 8 to 12 were complemented. A dual time step approach was applied to compute the numerical solutions. 1200 physical time steps with 100 inner iterations each were carried out to gain a converged result. Lift, drag and transition location at different angles of attack are plotted in Fig. 20.

The lift has almost linear dependence on the angle of attack and is nearly independent from the critical N factor. As expected, there is an influence of the critical N factor on the drag distribution. There are several empirical correlations between N factor and turbulence level, such as $N_{\text{crit}} = -8.43 - 2.4\ln(\text{Tu})$, validated by Arnal [35]. The higher the critical N factor, the lower the corresponding freestream

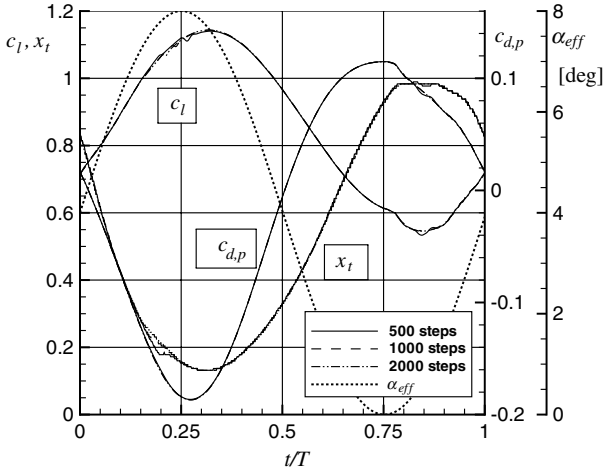

Fig. 17 Convergence of lift, drag and transition location for 500, 1000, and 2000 physical time steps per flapping period; flapping motion with $k = 0.2$, $Re = 100000$.

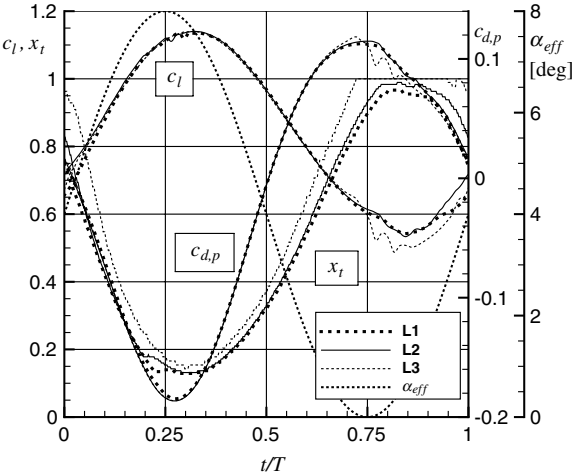

Fig. 19 Convergence of lift, drag and transition location for different grid levels; L1 is the finest level with 1088 × 224 cells, flapping motion with $k = 0.2$, $Re = 100000$.

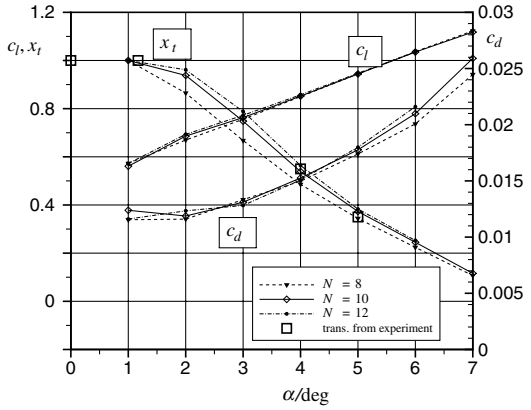

Fig. 20 Numerical computation of lift, drag and transition location for different angles of attack; $Re = 100000$, steady conditions.

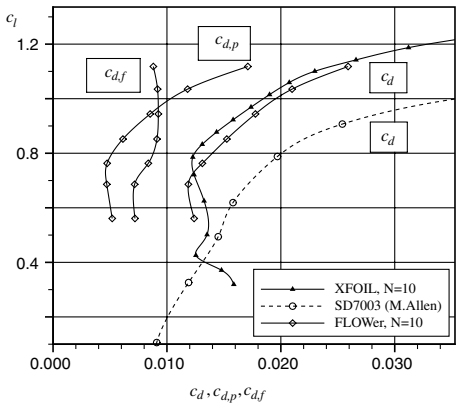

Fig. 21 Drag polar of the SG04 airfoil; $Re = 100000$, steady conditions and additional SD7003 data [36].

turbulence level. Hence, the disturbance waves are smaller and the transition takes place later resulting in larger laminar separation bubbles. Large LSB's increase the displacement thickness of the boundary layer and thus increase the drag. Notably, the transition location is also of great interest, i.e., the larger the angle of attack, the closer the transition position to the leading edge. Figure 21 shows the drag polar of the SG04 airfoil for the critical N factor of 10 computed by FLOWer and XFOIL. Although XFOIL is a very simple tool to predict steady airfoil aerodynamics, its polar is in good agreement with the results of the more complex FLOWer solver. Additionally, the drag decomposition into friction and pressure drag is plotted, which are approximately the same order of magnitude in this low Reynolds number range. Considering the small pressure drag values, the design goal of the SG04 airfoil with small laminar separation bubbles was attained. To be able to compare the polar with a SD7003 airfoil at an equivalent Reynolds number, experimental data from Selig et al. [36] is added to the chart. Mainly reasoned by the higher camber, the SG04 polar is shifted to higher lift values and has therefore a smaller drag at the same lift performance. However, the disadvantage of thin airfoils is clearly visible with a decreased operational range of lift. The transition behavior can be compared quantitatively with experimental data. See therefore Fig. 22, an oil flow picture taken in the wind tunnel at an angle of attack of 5 deg and equivalent Reynolds number. Visualization with oil flow pictures at the low wind-tunnel speed of 8 m/s was quite demanding because of the small shear stresses occurring. For this purpose, a special mixture containing titanium dioxide and low viscosity oils (e.g., Shell Macron EDM 110) was adapted**. The smooth region in the left-most 20% of the figure is a reflection of the ultraviolet light source. The oil flow picture clearly demonstrates the two dimensionality of the flow along the airfoil surface. It also contains the location of transition, which can be determined to approximately $x_t/c|_{5\ \mathrm{deg,oil}} = 0.35$ and agrees quite well with the numerical result of $x_t/c|_{5\ \mathrm{deg,num}} = 0.37$.

Furthermore, PIV measurements of the boundary layer were performed under steady conditions for 0, 1.17, and 4 deg angles of attack. Two of these results with their distribution of the turbulent shear stress σ_{xz} are displayed in Fig. 23††. The turbulent shear stress characterizes the viscous momentum transport across the boundary layer and can be used to detect regions of turbulent flow. Thus, the transition location in the measurements can be defined as the beginning of the turbulent wedge that starts from the shear layer of the LSB. To avoid errors in its localization due to insufficient resolution of flapping of the laminar part of the LSB, the point where the normalized Reynolds shear stress $-\overline{u'w'}/U_\infty^2$ reaches 0.1% and demonstrates a clearly visible rise is defined as the transition position. Hence, the transition location from the PIV measurements at 1.17 and 4 deg in Fig. 23 can be determined to $x_t/c|_{1.17\ \mathrm{deg,PIV}} = 1$ and $x_t/c|_{4\ \mathrm{deg,PIV}} = 0.55$, respectively. This corresponds very well with the results of the URANS computations, see Fig. 20.

3. *Oscillating Airfoil with $k = 0.2$*

A motion case for the oscillating airfoil with a reduced frequency of $k = 0.2$ was selected for the validation according to data from Pennycuick [21] and Herzog [22]. Hence, the interesting aspect of aerodynamic unsteadiness of the flapping motion is included in this case. Table 1 displays the detailed parameters. The plunging amplitude was adjusted to the upper bound of the motion apparatus. The mean angle of attack was set to 4 deg to produce sufficient lift in one flapping cycle ($\bar{c}_L = 0.85$). The flow case is typical for cruise flight of a bird in that a moderate amount of net thrust $c_T = 0.008$ is produced, according to the simulations presented below. Net thrust is the sum of thrust and drag, considering that these individual forces can only be separated artificially, see Windt and Radespiel [31].

The numerical simulations for this case were done by setting the freestream Mach number to 0.05. Low-speed preconditioning was performed. A dual time stepping scheme was used for the time-accurate computations which were carried out on the second grid level with 544×112 cells. A temporal resolution of 1000 physical time steps per period was defined.

In a first step, the steady transition prediction scheme was applied for three different critical N factors. The transition plot over one flapping period is depicted in Fig. 24. Herein, the diamonds indicate the transition location obtained by PIV measurements, which are presented beneath. It can be seen that the plots with higher critical N factors have their transition location further downstream. This behavior is as expected: the higher the critical N factor, the lower the turbulence level, the more time disturbance waves need to grow resulting in an increased laminar flow length. As for the cases of

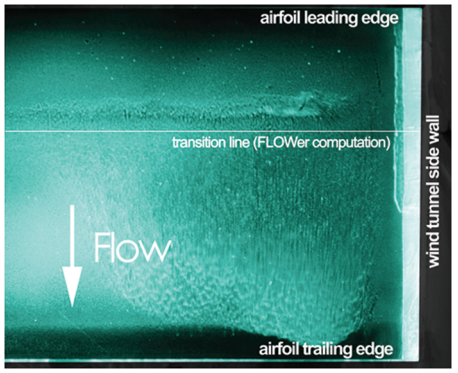

Fig. 22 Oil flow visualization of the SG04 airfoil at steady conditions; AoA = 5 deg, $Re = 100000$.

**Private communication with A. Liberatoscioli, "Force Measurements and Cross-Flow Estimation on a Flapping Bird-Like Airfoil," Student Research Project, No. 539, Institute of Fluid Mechanics, TU-Braunschweig,

††Private communication with A. Pascual Massana, "Particle Image Velocimetry (PIV) Measurements on a Bird-Like Airfoil," Student Research Project, No. 533, Institute of Fluid Mechanics, TU-Braunschweig.

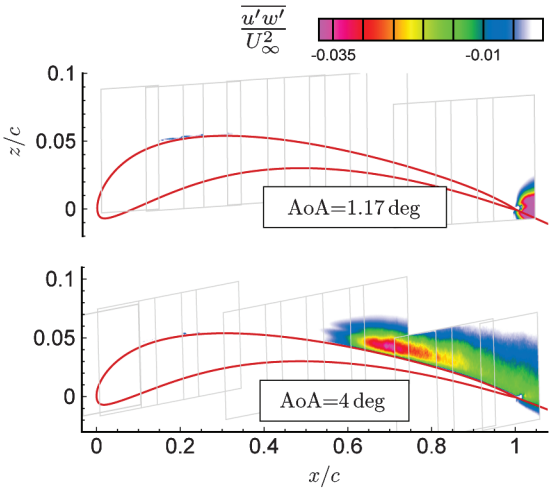

Fig. 23 PIV measurement of the turbulent shear-stress distribution σ_{xz} for two angles of attack at steady conditions, $Re = 100000$.

steady angles of attack, a critical N factor of 10 for the numerical simulations shows the best agreement with experimental transition data. From the inviscid theory of oscillating plates of Küssner [37] and Theodorsen [38], a phase lag between effective angle of attack and lift distribution is well known. The present computation shows that such a phase lag is also visible in the transition position, see the steady transition distribution in Fig. 24.

The transition prediction can be slightly improved using the unsteady transition prediction described in chapter 4D, see Fig. 25. Notably the transition at the top dead center of the motion is better reproduced. Nevertheless, the transition at $t/T = 0.5$ and $t/T = 0.625$ is only represented with an accuracy of 15%. One possible reason is solid-borne sound generated by high-frequency vibrations of the flapping flight motion apparatus. At the present time, it is not clear how much these boundary disturbances influence the transition process of the flapping airfoil. Other reasons could be modelling errors in production and dissipation of the applied Menter-Baseline turbulence model. The dash-dot line in Fig. 25 highlights the maximum speed of transition movement during the relaminarization process at $t/T = 0.625$ assuming that the turbulence convects downstream with 60% of the boundary-layer edge velocity in absence of any turbulence production or dissipation. This convective speed was recovered from the group velocity output of the linear stability solver LILO at the numerically-determined transition location $x_{t,\mathrm{num}}|_{t/T=0.625} \approx 0.6$, where the dash-dot line intersects the numerical transition solution. Note that the gradient of this line is larger than the gradient between the adjacent experimental transition locations.

Figure 26 affirms partially the hypothesis of modeling errors of the turbulence model. Herein, the turbulent shear-stress distributions σ_{xz} from the PIV experiments and the numerical computations are illustrated for four different phase angles starting from $t/T = 0$ at the top dead center. Derived from the Boussinesq approximation the relation

$$\overline{u'w'} = -\frac{\mu_t}{\varrho}\left(\frac{\partial \bar{u}}{\partial z} + \frac{\partial \bar{w}}{\partial x}\right) \tag{13}$$

Table 1 Motion parameters for the case of the oscillating airfoil

Reynolds number	$Re = 100,000$
Reduced frequency	$k = 0.2$
Chord length	$c = 0.2$ m
Geometric mean AOA	$\varphi_0 = 4$ deg
Amplitude of effective AOA	$\Delta\alpha_{\mathrm{eff}} = 4$ deg
Plunging amplitude	$\hat{z} = 0.1$ m
Pitch-plunge phase difference	$\Delta\Psi = 90$ deg

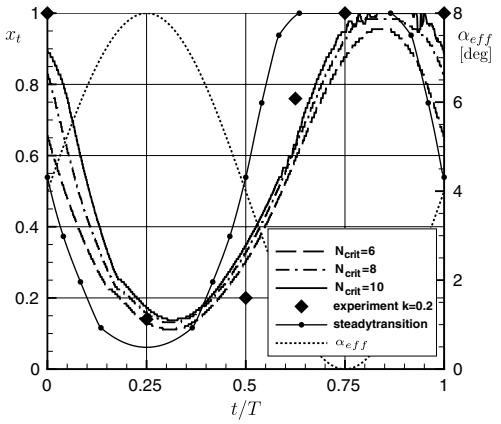

Fig. 24 Comparison of the steady transition prediction for different critical N factors with experimental data; flapping airfoil with $k = 0.2$.

was used to recover the turbulent shear stress from the URANS solution. Numerical simulations and experimental results are generally in good agreement. However, a closer look to the results at the middle of the downstroke ($t/T = 0.25$) implies that the flux in the experiment contains more turbulent kinetic energy than predicted in the numerical computation. Indeed, for thin shear layers, Bradshaw suggested a relation between turbulent kinetic energy and turbulent shear stress in its original notation given by $\overline{u_1 u_2} = aq^2$ wherein a is a function of the wall distance [39]. This excess of turbulent kinetic energy needs more time to dissipate to perform the relaminarization process. Consequently, the transition at $t/T = 0.5$ in the experiment is found further upstream than in the numerical solution, see also Fig. 25. It will be interesting to see the performance of Reynolds-stress turbulence models for this strongly nonequilibrium flow case and especially their impact on the speed of the relaminarization process for $0.6 \leq t/T \leq 0.75$.

Besides the comparison of the transition, also vortex shedding can be considered as a validation criterion. Depicted in Fig. 27 on the left is the lift distribution over one flapping cycle as a result of the URANS computation. Past the middle of the upstroke, some minor oscillations are visible which can be related to a frequency of 124.7 Hz. They are in relation with the frequency content of the amplified disturbance waves determined by the linear stability solver LILO. The physical background of these oscillations is a complex interaction between the Tollmien–Schlichting and the Kelvin–Helmholtz transition process along the laminar separation bubble, which could be resolved due to the small physical time step size of the numerical computation. On the right hand side of the picture, an instantaneous image of the wake of the flapping airfoil was captured with standard PIV at a phase of 320 deg ($t/T = 0.89$). Illustrated is the nondimensional vorticity, given by

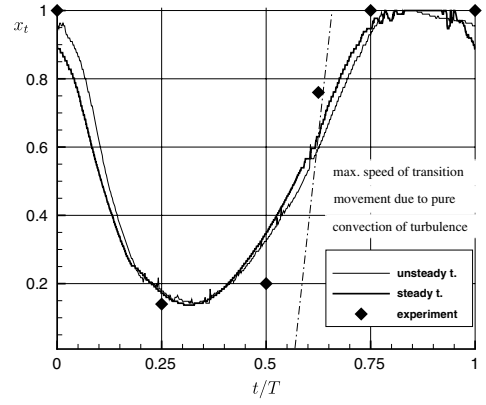

Fig. 25 Comparison of the steady and unsteady transition prediction for a critical N factors of 10 with experimental data; flapping airfoil with $k = 0.2$.

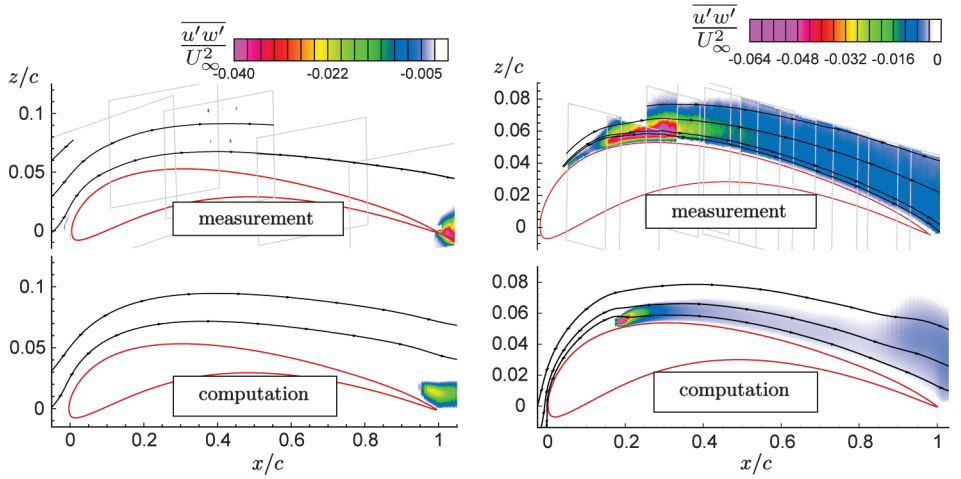

a) Top dead center, $t/T = 0$, $\alpha_{eff} = 4$ deg

b) Mid downstroke, $t/T = 0.25$, $\alpha_{eff} = 8$ deg

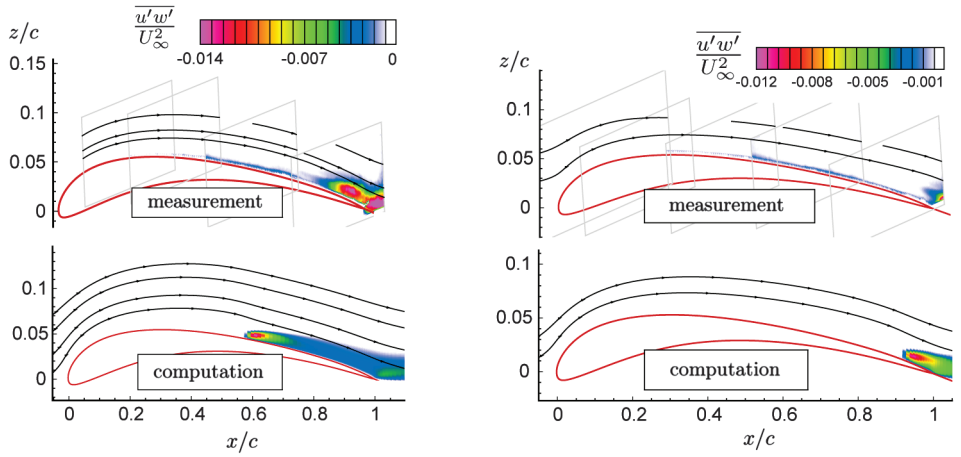

c) During upstroke, $t/T = 0.625$, $\alpha_{eff} = 1.17$ deg

d) Mid upstroke, $t/T = 0.75$, $\alpha_{eff} = 0$ deg

Fig. 26 Comparison of the turbulent shear-stress distribution between numerical computation and experimental results.

$$\frac{\omega^f}{U_\infty/c} = \frac{1}{U_\infty/c} \cdot \left(\frac{\partial w}{\partial x} - \frac{\partial u}{\partial z} \right) \tag{14}$$

Notably, there are large regular vortex structures shed downstream with a transport velocity of about 5 m/s yielding a shedding frequency of about 154 Hz, a good agreement with the numerical simulation. The instantaneous flowfield image was chosen because slight changes in the disturbances of the oncoming flow during every flapping cycle will impact the vortex-shedding process. Therefore, the vortices have an uncertainty in their location and will not persist in the flowfield after ensemble averaging.

B. Flexible Airfoil

The coupling environment with its numerical elements was validated for different aeroelastic problems in transonic and hypersonic flow, see [10,16,33]. Dealing now with incompressible fluid flow, no special requirement for the coupling environment needs to be considered.

The fluid grid used for this computation is composed of 584×128 cells and was originally generated based on the SG04 airfoil. Because of the geometric difference of both the aerodynamic and the structural model, this fluid grid needs to be adapted for the structural model of Fig. 6a, i.e., the rear part of the SG04 airfoil shape was simplified to a flat plate. This minor design change can be accepted because the main aerodynamic performance of the airfoil at this low Reynolds number range is defined by the leading edge and the subsequent 40% of the airfoil shape. Using the same interpolation for the surface coordinates as for the surface deformation from Eq. (9), as well as the grid deformation described through Eq. (11), a body-fitted fluid grid could be generated, see Fig. 13b.

The finite element model of the structure, also depicted in Fig. 13b in red, was validated in terms of the first eigenfrequency, eigenform and mass, see Fig. 28. To measure the first eigenfrequency and eigenform of the flexible airfoil, the model was excited with different frequencies and a small amplitude at the quarter chord line, i.e., only deformations due to inertial loads were considered. The amplitude of the excitation was kept small to reduce the influence of the surrounding air, i.e., the air inside the rig with the flexible airfoil was not evacuated for these measurements. The deformation was first measured via a laser sensor, which uses optical triangulation as a measuring principle at specified points, see Unger et al. [20] for details. These measuring points are depicted in Fig. 28a as vertical lines together with the reconstructed eigenform. The reconstructed eigenform was determined with the aid of a surface spline and from this eigenform a good 2-D behavior can be observed, i.e., the deformation is a spanwise-uniform pure first bending mode of the airfoil mean line. This eigenform corresponds to a eigenfrequency of $f_1^{ex} = 14.8$ Hz, which was obtained from the mean amplitude versus frequency plot, Fig. 28c, where the mean amplitude was calculated from the amplitude at these five measuring points, which are situated near the trailing edge. Additionally, the form at this eigenfrequency was measured with the optical 3-D deformation measuring system (ARAMIS), Fig. 28b, which gives identical results to the form obtained with laser sensor at the 16 measuring points from Fig. 28a. It should be noted that with both approaches, the laser sensor system and ARAMIS, the exact trailing-edge deformation cannot be obtained. The laser sensor system uses discrete points in space to

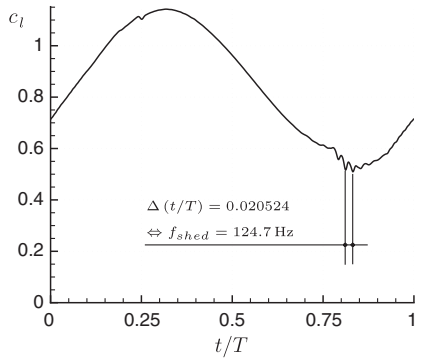

a) Oscillations in the lift distribution

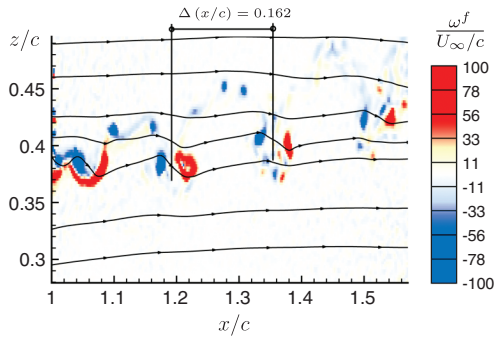

b) Vortex shedding in the wake of the oscillating airfoil

Fig. 27 Comparison between numerical predicted and experimental measured vortex shedding.

which the distance is measured and a deforming trailing edge is not fixed in this space. ARAMIS uses discrete voxels in which the captured images are divided and the trailing edge is usually not on the voxel's edge. The first eigenform of the finite element model is depicted in Fig. 28d, which is in very good agreement with the measured eigenform. The corresponding eigenfrequency was computed to $f_1^{\mathrm{fem}} = 14.7$ Hz, which is very close to the experimentally obtained eigenfrequency. Finally the mass was simply validated by comparing the mass of the wind tunnel and the finite element models, which both are $m^{\mathrm{ex}} = m^{\mathrm{fem}} = 124$ g.

Taking the experience of the rigid airfoil for the oscillating airfoil into account, 500 physical time steps per period were used and converged results for lift, drag and transition location were obtained after three flapping periods. For turbulence modeling, the Menter-Baseline model was used, due to reasons of improved computation stability, the steady transition prediction was applied with a critical N factor set to 8.

1. *Results for Steady Conditions*

A steady computation was used to calculate the jig-shape of the structural model, which is needed for the design of the wind-tunnel model. The jig-shape is the shape of the airfoil that is unaffected by any inertial or aerodynamic forces, i.e., the shape of the airfoil in rest without fluid flow around it. To obtain the aerodynamic shape of the original aerodynamic airfoil, a gliding flight with a Reynolds number of $Re = 100000$ and angle of attack $\alpha = 3$ deg is assumed. To get the jig-shape of the airfoil, an iteration process similar to that described above is carried out, where the residual is taken as the difference to the original SG04 airfoil.

In Fig. 29a the jig-shape is depicted as the black boundary line. The pressure distribution of the fluid flow around the airfoil is also seen in this figure and the pressure distribution on the airfoil surface is depicted in Fig. 29b. The displacement at the trailing edge is calculated to be 3.5% of the chord length. The location of the transition on the upper side of the airfoil is calculated to lie at $x_t/c = 0.66$. This also can be seen from Fig. 29b, where the transition point is indicated by the strong pressure rise on the upper surface at this location. The resulting turbulent reattachment occurs at a location 71% of the chord length. The dimensionless velocity contours are shown in Fig. 29c together with streamlines indicating the laminar separation bubble. The corresponding $\overline{u'w'}$ contours are shown in Fig. 29d.

2. *Oscillating Airfoil with $k = 0.2$*

For the oscillating airfoil the same motion parameters were used as described in Table 1. The time history of lift and drag as well as transition position on the upper airfoil side x_t are shown in Fig. 30. The flapping configuration produces lift during the whole cycle. Maximum lift is obtained shortly after the middle of the downstroke. Thus, the lift does not peak at the largest effective angle of attack of 8 deg at $t/T = 0.25$. There is rather a delay between maximum lift and maximum effective angle of attack due to unsteady effects. This delay is also visible through the smallest lift coefficient, which occurs shortly after the smallest effective angle of attack of 0 deg at $t/T = 0.75$. The drag coefficient plot indicates negative drag during the whole downstroke of the airfoil motion, i.e., the thrust is produced in this part of the cycle. Checking the drag coefficient values of the upstroke, one notices that their magnitude is in sum smaller than the thrust generated during the downstroke. Hence, the flapping motion generates a net thrust.

Similar to the rigid airfoil, it can be seen clearly from the transition plot that the laminar separation bubble moves from the rear part of the airfoil to the stiff forebody during the downstroke ($0 \leq t/T \leq 0.5$). Shortly before the bottom dead center, the transition point moves back again to the rear part of the airfoil during the upstroke ($0.5 \leq t/T \leq 1.0$), while it never reaches the last 30% of the rear part, i.e., the laminar separation bubble is present all time for the flapping flexible airfoil. This is indeed a different behavior compared with the rigid airfoil where the laminar separation bubble vanished in the last part of the upstroke ($0.75 \leq t/T \leq 1$). The diamonds in the plot refer to the experimental measurements of the transition location by calculation of the turbulent shear-stress distribution, see also Fig. 31.

The measured transition is in agreement with the numerical prediction. However, the experimentally determined transition locations for $0.6 < t/T < 1.0$ are situated significantly further downstream. This finding is in agreement with the transition behavior found for the rigid airfoil in Fig. 24. The rapid downstream movement of transition experimentally observed during the early part of the upstroke is not reproduced by the combined present model of transition and turbulence. As already observed with the rigid airfoil, there seems to be a modeling error in production, convection and dissipation of turbulence. It is hoped that the source of the observed discrepancies will be identified in future research work using further URANS simulations with Reynolds-stress turbulence modeling and also large eddy simulations. Based on the experience gained from many runs of the current code, we feel that the important parameters for the propulsive efficiency estimation, lift and drag, will not be influenced significantly. This conclusion is confirmed by computations at different critical N factors which effected the transition distribution. According to this comparison, a critical N factor of 6 yields a propulsive efficiency of 81%, whereas an efficiency of 83.5% is achieved with the critical N factor of 10.

Validation of the predicted fluid structure interactions is possible by using the structural deformations. With two measurement techniques, the commercially available ARAMIS system and the custom made system described in the above section, a complete airfoil surface deformation field could be determined at different phase angles. From these data, the deformation of the jig-shape in chordwise direction could be extracted, and this is shown exemplarily at four different phase angles for the custom made experiment, see Fig. 32. The data points are connected with polynomial fits. The fitting curve was extrapolated until $x/c = 1$ and could resolve the problem of missing deformation data near the trailing edge due to poor image pattern correlation. The plots reveal the largest deformation when the airfoil has passed the top dead center of the motion, i.e., the airfoil has then the smallest camber.

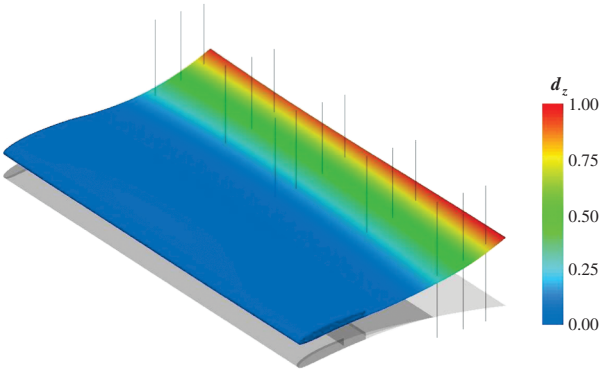

a) First eigenform obtained with laser sensor reconstructed from the deformation obtained with laser sensor at 16 measuring points (indicated as vertical lines) at f_1^{ex} = 14.8 Hz

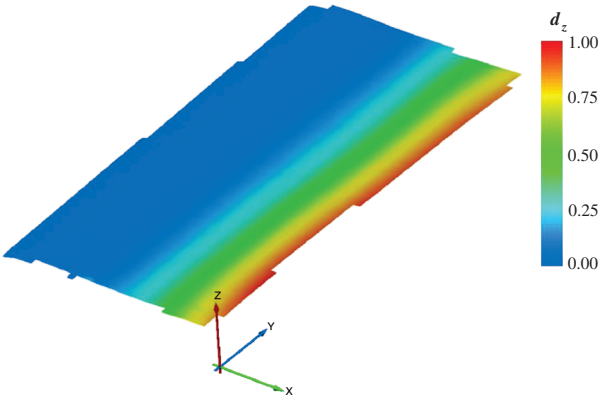

b) First eigenform obtained with ARAMIS at f_1^{ex} = 14.8 Hz

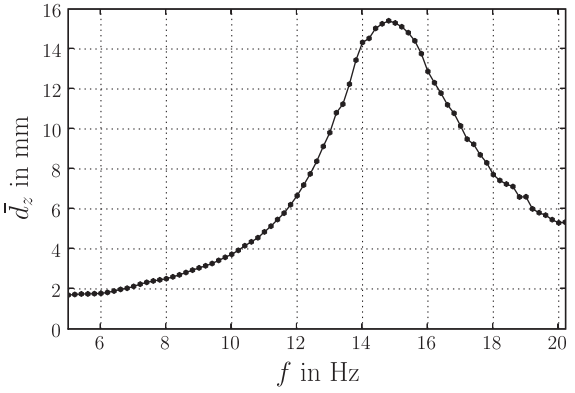

c) Amplitude vs. frequency, whereby the amplitude was averaged from the deformation at the five measuring points near the trailing edge from (a)

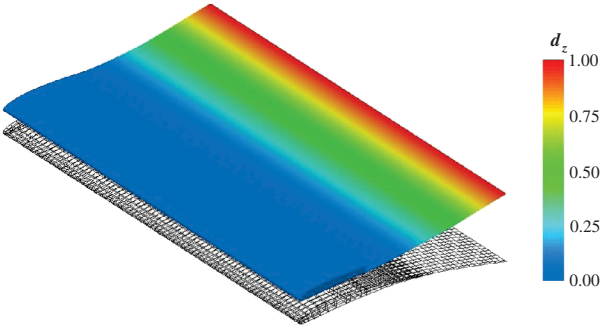

d) First eigenform computed with FEM at f_1^{fem} = 14.7 Hz

Fig. 28 First eigenform and eigenfrequency of the structural model.

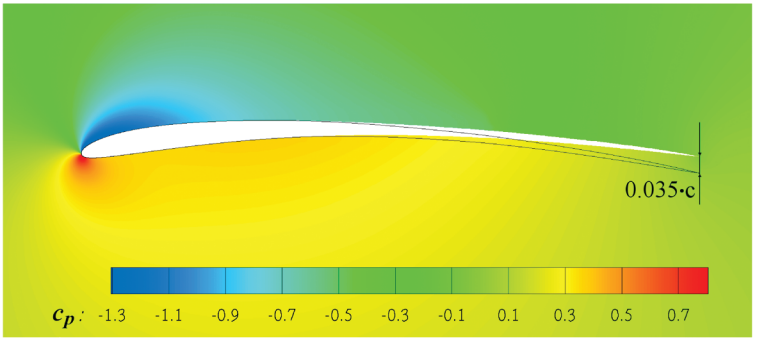

a) Pressure contours together with the jig-shape of the airfoil

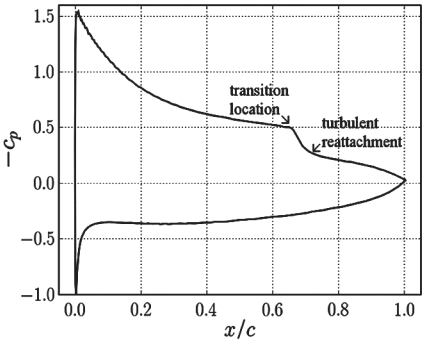

b) Pressure distribution on the deformed airfoil

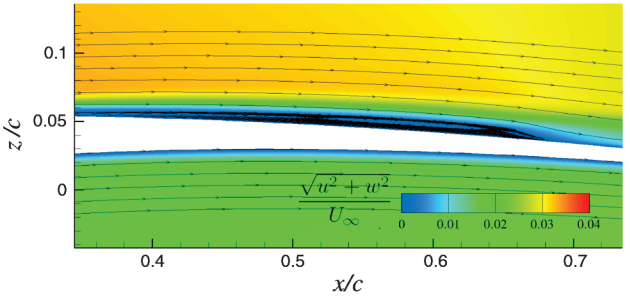

c) Dimensionless velocity contours and streamlines

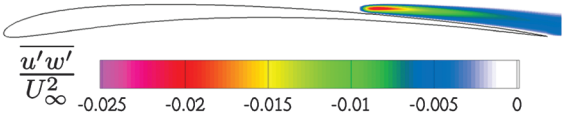

d) $\overline{u'w'}$-contours

Fig. 29 Analysis of the airfoil in gliding flight ($Re = 10^5$, $\alpha = 3$ deg).

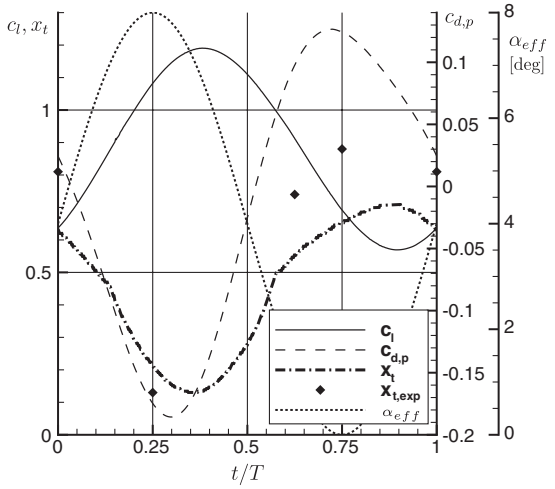

Fig. 30 Lift, pressure drag and transition location of the flapping flexible airfoil.

During the downstroke the camber is continuously increasing until the bottom dead center is reached. This deformation behavior is a result of the partially counteracting forces of inertia and lift.

From an aerodynamic point of view, this behavior is favorable because the downstroke is known to be the thrust producing part of the flapping cycle. According to the linear airfoil theory, increased camber means increased lift and consequently thrust due to the Knoller–Betz effect. Hysteresis effects due to the unsteadiness of the investigated flapping case cause a delay in the increased thrust production. Also, the deformation behavior of the upstroke is aerodynamically advantageous because the decreasing camber reduces the drag of this configuration.

A comparison of the trailing-edge deformation between numerical simulation and experimental data is also given in Fig. 32. Both data of the commercial available system (ARAMIS) and the custom made deformation measurement system are depicted. It can be seen that the deformations are always positive. This basically means that at the top dead center, both loads, inertia and aerodynamic loads, accumulate to result in the high deformation, while at the bottom dead center both forces nearly cancel each other out, which results in the low deformation. Thus the second requirement on deformation within the structural design process is satisfied, i.e., it was requested that the deformations due to aerodynamic and inertia loads should be in same range. The general deformation behavior is well resolved with the numerical simulation. However, the numerical result predicts slightly higher deformations. The largest error is about 2 mm at bottom dead center. This discrepancy has three sources. Firstly, with the ARAMIS system it is impossible to resolve exactly the trailing-edge deformation due the use of uniform voxels in which the obtained images are resolved. Secondly and a more important source is the accuracy of the model's jig-shape. Because of the use of orthotropic material for curved shells and the layer structure of Fig. 7, manufacture related initial stresses are unavoidable, which results in spanwise distortion. The deviation of the vertical trailing-edge position due to the curvature of the structural model is temperature dependent and is about 1.0–1.5 mm in the spanwise direction. This is even further intensified due to the anticlastic deformation of the trailing edge, which is nonneglegible due to the geometry of the manufactured model (the span has twice the length of the chord). A third source of the discrepancy is the presence of the wind-tunnel walls, which are not modeled in the computations.

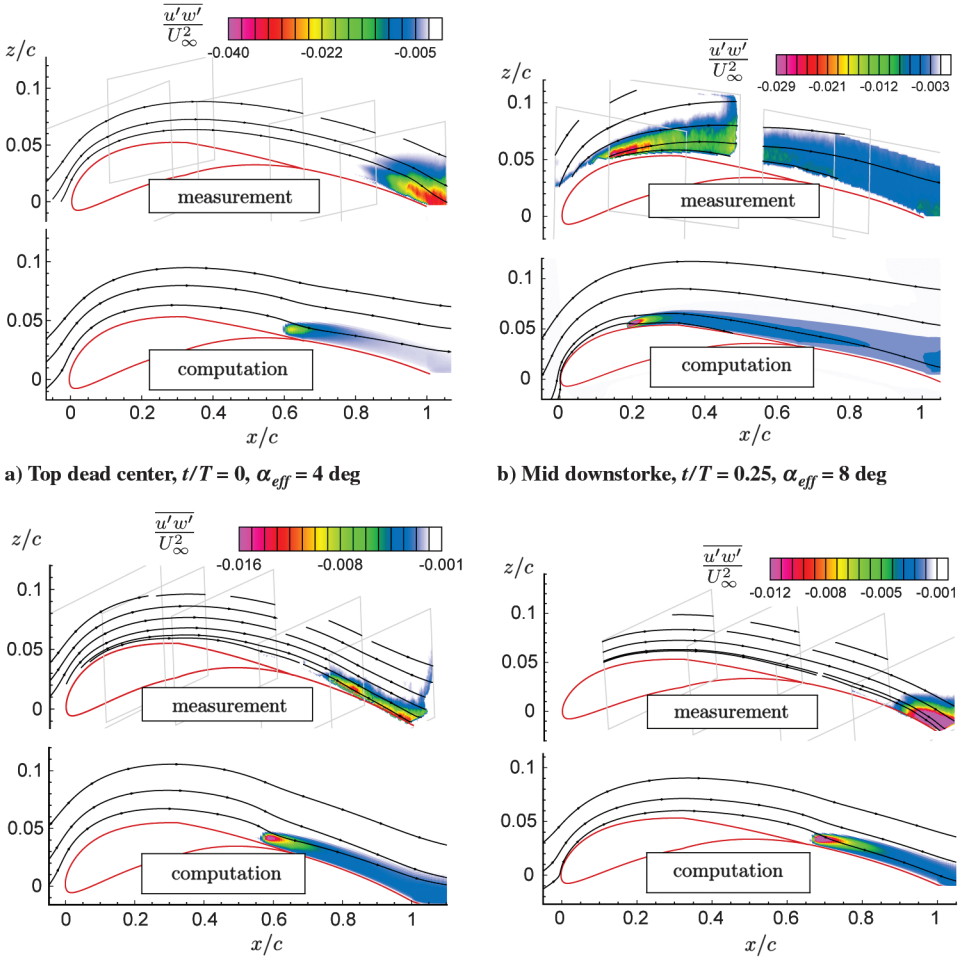

a) Top dead center, $t/T = 0$, $\alpha_{eff} = 4$ deg

b) Mid downstroke, $t/T = 0.25$, $\alpha_{eff} = 8$ deg

c) During upstroke, $t/T = 0.625$, $\alpha_{eff} = 1.17$ deg

d) Mid upstroke, $t/T = 0.75$, $\alpha_{eff} = 0$ deg

Fig. 31 Comparison of the turbulent shear-stress distribution between numerical computations and experimental results.

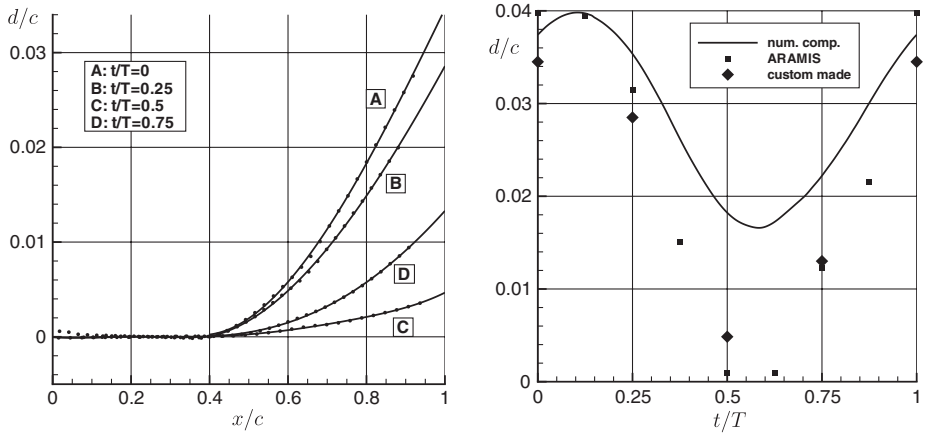

a) Deformation of the jig-shape chord line (custom made deformation measurement system)

b) Comparison between numerical method and experimental result

Fig. 32 Comparison of the deformation of the trailing edge between numerical computation and experimental results.

3. Brief Comparison Between Rigid and Flexible Airfoils

Having validated the computational methods for rigid and flexible flapping airfoils, the lift, drag and transition results can be compared for the validation case, see Fig. 33. To ensure a fair comparison, both computations were performed with a steady transition prediction using a critical *N* factor of 8. The lift plots indicate positive lift during the whole flapping cycle for both airfoils. By integrating the lift coefficient over time, the rigid airfoil generates with $c_{l,\text{mean}} = 0.85$ nearly the same mean lift as the flexible airfoil with its value of 0.88. At the middle of the downstroke, the maximum effective angle of attack with its value of 8 deg is reached. According to unsteady effects, the maximum lift is obtained with a certain phase delay. For the case of the flexible airfoil this delay is larger and can be explained by the trailing-edge deformation of the airfoil. During the downstroke, the deformation causes a continuous increase of the airfoil camber to higher lift coefficients. As already shown in Fig. 32, the maximum cambering is present near bottom dead center.

Considering the drag plots of the airfoils, one can also integrate their distributions over one flapping period to determine a mean drag value. A negative sign of this value denotes a net thrust per flapping cycle. It has to be mentioned that net thrust is consequently the sum of drag and thrust generated by the flapping airfoil. For the flexible airfoil, the net thrust has a value of $-c_{d,\text{mean}} = 0.004$ and is in the same range as for the rigid airfoil with a value of 0.008. For both cases the drag for the airfoil under steady conditions with a value of 0.015 at the mean geometric angle of attack of the flapping motion can be overcome. The results indicate that the motion parameters and the structural design parameters for the flexible airfoil should be carefully adjusted together so that thrust and propulsive efficiency take advantage of the fluid-structure interaction. To improve the net thrust for the flexible airfoil, the usage of actuators is advantageous. These actuators could be used to change actively the camber of the airfoil during a flapping period. For example, the actuators can work in a way such that they increase the camber during the downstroke to produce more thrust and to decrease the camber during the upstroke to reduce the drag.

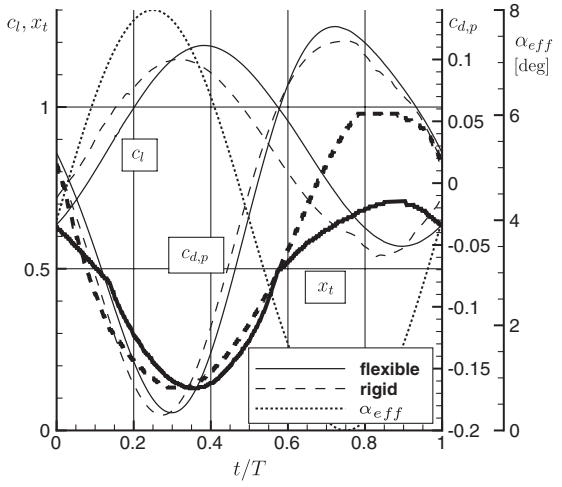

Fig. 33 Comparison of lift, pressure drag, and transition location for the flapping airfoils (numerical computations).

VII. Conclusions

We consider a newly developed birdlike airfoil, referred to as the SG04, oscillating with a nominally two-dimensional combined pitch-plunge motion at a reduced frequency of $k = 0.2$ in the transitional Reynolds number range of 100,000. The long-term question to answer is whether airfoil flexibility can have a positive impact on the propulsive efficiency. We set up a sophisticated numerical computation scheme based on an unsteady RANS solver linked with a structural solver using a Galerkin method. To validate the numerical simulations, the boundary layers of a rigid and a flexible flapping airfoil model were investigated with high-resolution stereoscopic PIV. Good agreement in the flow prediction has been demonstrated. The Menter–Baseline turbulence model delivers generally adequate results for the turbulence intensity resulting in a reasonable prediction of the transition caused by laminar separation bubbles. However, systematic discrepancies between simulation and experiment were found regarding the speed and position of the transition during the upstroke of the airfoil. The deformations that result from aerodynamic and inertial loads upon the flexible airfoil structure were well reproduced by the simulations. The results demonstrate that the numerical simulation schemes provided in this contribution may be deemed as acceptable tools for conceptualization and parametric studies to understand the influence of wing flexibility of natural flyers.

Acknowledgments

As a part of the priority program SPP 1207, this project is funded by the German Research Foundation. The authors thank C. J. Kähler, E. Mazlum, J. Windte, and D. Rival for valuable discussions and their support.

References

[1] Dickinson, M. H., and Goetz, K. G., "Unsteady Aerodynamic Performance of Model Wings at Low Reynolds Numbers," *Journal of Experimental Biology*, Vol. 174, No. 1, 1993, pp. 45–64.

[2] Mueller, T. J., *Fixed and Flapping Wing Aerodynamics for Micro Air Vehicle Applications*, Vol. 195, Progress in Astronautics and Aeronautics, AIAA, Reston, VA, 2001.

[3] Ol, M., Bernal, L., Kang C.-K., and Shyy, W., "Shallow and Deep Dynamic Stall for Flapping Low Reynolds Number Airfoils," *Experiments in Fluids*, Vol. 46, No. 5, 2009, pp. 883–901. doi:10.1007/s00348-009-0660-3

[4] Heathcote, S., and Gursul, I., "Flexible Flapping Airfoil Propulsion at Low Reynolds Numbers," *AIAA Journal*, Vol. 45, No. 5, 2007, pp. 1066–1079. doi:10.2514/1.25431

[5] De Luca, A., Reeder, M., Freeman, J., and Ol, M., "Flexible- and Rigid-Wing Micro Air Vehicle: Lift and Drag Comparison," *Journal of Aircraft*, Vol. 43, No. 2, 2006, pp. 572–575. doi:10.2514/1.15643

[6] Lian, Y., and Shyy, W., "Laminar-Turbulent Transition of a Low Reynolds Number Rigid or Flexible Airfoil," AIAA Paper 2006-3051, 2006.

[7] Radespiel, R., Windte, J., and Scholz, U., "Numerical and Experimental Flow Analysis of Moving Airfoils with Laminar Separation Bubbles," *AIAA Journal*, Vol. 45, No. 6, 2007, pp. 1346–1356. doi:10.2514/1.25913

[8] Buchholz, J., and Smits, A., "The Wake Structure and Thrust Performance of a Rigid Low-Aspect-Ratio Pitching Panel," *Journal of Fluid Mechanics*, Vol. 603, 2008, pp. 331–365.

[9] Koochesfahani, M., "Vortical Patterns in the Wake of an Oscillating Airfoil," *AIAA Journal*, Vol. 27, No. 9, 1989, pp. 1200–1205. doi:10.2514/3.10246

[10] Unger, R., Haupt, M. C., and Horst, P., "Application of Lagrange Multipliers for Coupled Problems in Fluid and Structural Interactions," *Computers and Structures*, Vol. 85, Nos. 11–14, 2007, pp. 796–809. doi:10.1016/j.compstruc.2007.01.006

[11] Spalart, P., and Strelets, M., "Mechanisms of transition and heat transfer in a separation bubble," *Journal of Fluid Mechanics*, Vol. 403, 2000, pp. 329–349. doi:10.1017/S0022112099007077

[12] Rist, U., "Instability and Transition Mechanisms in Laminar Separation Bubbles," NATO Research and Technology Organization Applied Vehicle Technology–Von Karman Institute Lecture Series 104, 2003.

[13] Oertel, H., and Delfs, J., *Strömungsmechanische Instabilitäten*, Springer, Berlin, 1996.

[14] Bilo, D., "Flugbiophysik von Kleinvögeln; II. Kinematik und Aerodynamik des Flügelaufschlages beim Haussperrling," Ph.D. Dissertation, Zoologisches Institut der Universität München, 1970.

[15] Farhat, C., van der Zee, K. G., and Geuzaine, P., "Provably Second-Order Time-Accurate Loosely-Coupled Solution Algorithms for Transient Nonlinear Computational Aeroelasticity," *Computer Methods in Applied Mechanics and Engineering*, Vol. 195, Nos. 17–18, 2006, pp. 1973–2001. doi:10.1016/j.cma.2004.11.031

[16] Haupt, M. C., Niesner, R., Unger, R., and Horst, P., "Computational Aero-Structural Coupling For Hypersonic Applications," AIAA Paper 2006-3252, 2006.

[17] Bilo, D., "Flugbiophysik von Kleinvögeln; I. Kinematik und Aerodynamik des Flügelabschlages beim Haussperrling," Ph.D. Dissertation, Zoologisches Institut der Universität München, 1970.

[18] Bansmer, S., Scholz, U., Windte, J., Kähler, C., and Radespiel, R., "Flow Field Measurements on an Oscillating Airfoil for Flapping Wing Propulsion," AIAA Paper 2008-581, 2008.

[19] Selig, M., *Low Reynolds Number Airfoil Design Lecture Notes*, VKI Lecture Series, Applied Vehicle Technology Panel, Nov. 2003

[20] Unger, R., Haupt, M. C., Horst, P., and Windte, J., "Structural Design and Aeroelastic Analysis of an Oscillating Airfoil for Flapping Wing Propulsion," AIAA Paper 2008-306, 2008.

[21] Pennycuick, C., "Wingbeat Frequency of Birds in Steady Cruising Flight: New Data and Improved Predictions," *Journal of Experimental Biology*, Vol. 199, No. 7, 1996, pp. 1613–1618.

[22] Herzog, K., *Anatomie und Flugbiologie der Vögel*, Gustav Fischer Verlag, Stuttgart, 1968.

[23] Byrne, D., Buchmann, S., and Spangler, H., "Relationship Between Wing Loading, Wingbeat Frequency and Body Mass in Homopterous Insects," *Journal of Experimental Biology*, Vol. 135, 1988, pp. 9–23.

[24] Raffel, M., Willert, C. E., Wereley, S. T., and Kompenhans, J., *Particle Image Velocimetry: A Practical Guide*, Springer–Verlag, New York, 2007.

[25] Hinze, J. O., *Turbulence: An Introduction to its Mechanism and Theory*, McGraw–Hill, New York, 1959.

[26] Kroll, N., Rossow, C. C., Schwamborn, D., Becker, K., and Heller, G., "MEGAFLOW: A Numerical Flow Simulation Tool for Transport Aircraft Design," International Council of the Aeronautical Sciences, Paper 1105, Toronto, 2002.

[27] Menter, F., "Two-Equation Eddy-Viscosity Transport Turbulence Model for Engineering Applications," *AIAA Journal*, Vol. 32, No. 8, 1994, pp. 1598–1605. doi:10.2514/3.12149

[28] Schrauf, G., LILO 2.1 User's Guide and Tutorial. GSSC Technical Report 6, Ver. 2.1, 2006.

[29] Van Ingen, J. L., "Suggested Semi-Empirical Method for the Calculation of the Boundary Layer Transition Region," Delft University of Technology Rept. VTH-74, Department of Aerospace Engineering, 1956.

[30] Schrauf, G., "Transition Prediction Using Different Linear Stability Analysis Strategies," AIAA Paper 94-1848-CP, 1994.

[31] Windte, J., and Radespiel, R., "Propulsive Efficiency of a Moving Airfoil at Transitional Low Reynolds Numbers," *AIAA Journal*, Vol. 46, No. 9, 2008, pp. 2165–2177. doi:10.2514/1.30569

[32] Windte, J.,Scholz, U., and Radespiel, R., "Validation of the RANS-Simulation of Laminar Separation Bubbles on Airfoils," *Aerospace Science and Technology*, Vol. 10, No. 6, 2006, pp. 484–494. doi:10.1016/j.ast.2006.03.008

[33] Unger, R., Haupt, M. C., and Horst, P., "Coupling Techniques for Computational Nonlinear Transient Aeroelasticity," *Journal of Aerospace Engineering*, Vol. 222, No. 4, 2008, pp. 435–447. doi:10.1243/09544100JAERO283

[34] Yuan, W., Khalid, M., Windte, J., Scholz, U., and Radespiel, R., "Computational and Experimental Investigations of Low-Reynolds-Number Flows Past an Airfoil," *The Aeronautical Journal*, Vol. 111, No. 1115, 2007, pp. 17–29.

[35] Arnal, D., "Boundary Layer Transition: Predictions Based on Linear Theory," *AGARD-VKI Special Course on Progress in Transition Modelling*, AGARD Rept. 793, 1994.

[36] Selig, M., Guglielmo, J., Broeren, A., and Giguére, P., *Summary of Low-Speed Airfoil Data*, Vol. 1, SoarTech Publications, Virginia Beach, VA, 1995.

[37] Küssner, H. G., "Zusammenfassender Bericht über den instationären Auftrieb von Flügeln," *Luftfahrtforschung*, Vol. 13, No. 12, 1936, pp. 410–424

[38] Theodorsen, T., "General theory of aerodynamic instability and the mechanism of flutter," NACA TM 496, 1935.

[39] Bradshaw, P., *Turbulence*, Springer–Verlag, New York, 1976.

[40] Horton, H., *Laminar Separation Bubbles in Two and Three Dimensional Incompressible Flow*, Department of Aeronautical Engineering, Queen Mary College, University of London, London, 1968.

[41] Oehme, H., "Vergleichende Profiluntersuchungen an Vogelflügeln," *Beiträge zur Vogelkunde*, Band 16, Heft 1/6, 1970.

M. Visbal
Associate Editor